Precambrian Research 347 (2020) 105857

Contents lists available at ScienceDirect

Precambrian Research

journal homepage: www.elsevier.com/locate/precamres

Geochronology, geochemistry, and Hf–Sr-Nd isotopes of the Hamisana Shear Zone granitoids in northeastern Sudan: Petrogenesis and tectonic evolution of neoproterozoic juvenile crust in the Nubian Shield

Adil Saeed[a,b,*], Zuoxun Zeng[a,c], Yildirim Dilek[d,1], S.F. Awadelseid[b], A.A. Abdel Rahman[b], Munir M.A. Adam[a]

[a] School of Earth Sciences, China University of Geosciences, Wuhan 430074, China
[b] College of Petroleum Geology and Minerals, University of Bahri, Khartoum 1660, Sudan
[c] Huazhong Tectonomechanical Res. Center, China University of Geosciences, Wuhan 430074, China
[d] Department of Geology & Environmental Earth Sciences, Miami University, Oxford, OH 45056, USA

ARTICLE INFO

Keywords:
U-Pb zircon age
Hf, Sr-Nd isotopes
Neoproterozoic Juvenile crust
Hamisana Shear Zone Granitoids
Arabian-Nubian Shield

ABSTRACT

We have investigated the petrology, U-Pb zircon ages, whole-rock geochemistry, and Hf–Sr-Nd isotopic compositions of the Hamisana Shear Zone granitoids (HSZG) in the Arabian-Nubian Shield (ANS) in northern Sudan in order to constrain their petrogenesis and tectonic setting of formation. The HSZG rocks consist mainly of granite, quartz syenite, and quartz monzonite that collectively make up two major groups based on their ages and geochemical compositions. The older group (average U-Pb zircon age of ~663 Ma) is represented by calc-alkaline and I-type peraluminous granites, whereas the younger group (average U-Pb zircon age 623.5 Ma) is characterized by A-type and metaluminous monzonitic intrusions. All rocks show high Al_2O_3, La/Nb, Th/Ta, Ba/Nb ratios, and similar REE patterns indicating enrichment of LILEs (Ba, K, Pb, and Sr) and depletion of HFSEs (Nb, Ta, Sm, P, and Ti), consistent with the characteristics of subduction-related magmas. La/Yb, La/Sm, Th/Nb, Rb/Sr, and Rb/Ba ratios suggest that magmas of the HSZG formed by partial melting of a subduction-modified mantle beneath the ANS. Sr-Nd isotopic compositions of both groups with Nd model ages of 794–877 Ma have εNd(t) values of +5.24 to +6.10. In-situ Hf isotope analyses indicate εHf(t) values of +10.36 to +10.90 for the older granites and +9.9 to +10.73 for the younger quartz monzonites. These isotopic features point to a depleted mantle source of their magmas with no involvement of Pre-Neoproterozoic crust in their melt evolution. The older HSZG granite suites represent pre-collision arc magmatism, whereas the younger HSZG quartz monzonite suites mark post-collisional magmatic units. Both magmatic events contributed significantly to juvenile crust construction during the Neoproterozoic assembly of the ANS.

1. Introduction

The Arabian-Nubian Shield (ANS) includes a series of juvenile arc terranes (Fig. 1), whose construction and amalgamation involved several major tectonic and magmatic events during the protracted East African Orogeny (950–550 Ma; Stern, 1994). Thus the ANS evolved through the accretion of intra-oceanic arc-trench systems (~700 Ma; Patchett and Chase, 2002; Stoeser and Frost, 2006; Khalil et al., 2015), several microcontinental collisions in the late Neoproterozoic (Kröner et al., 1987; Stern, 1994; Stein and Goldstein, 1996; Meert, 2003; Stoeser and Frost, 2006; Be'eri-Shlevin et al., 2011, therein), and post-collisional (~640–580 Ma) magmatism. The closure of the Mozambique Ocean marked the final stage of the East African Orogeny and the assembly of West Gondwana (Collins and Pisarevsky, 2005; Stern, 1994, 2002; Stern and Johnson, 2010; Johnson and Woldehaimanot, 2003). Development of some major transcurrent fault systems within the young East African Orogenic Belt modified the internal structure of the ANS considerably (Fig. 1; Kröner et al., 1987; Abdelsalam et al., 2003; Stern, 1994; Stern and Campins, 1996; Stern et al., 1989; Miller and Dixon, 1992; Stern, 1994; de Wall et al., 2001).

The basement rocks of the ANS represent predominantly Neoproterozoic juvenile crust, which developed through differentiation and crystallization of upper mantle-originated melt without any significant contamination by pre-existing continental crust (Stern, 1994;

* Corresponding author at: School of Earth Sciences, China University of Geosciences, Wuhan 430074, China.
E-mail addresses: adil.geology@gmail.com (A. Saeed), dileky@miamioh.edu (Y. Dilek).
[1] 0000-0003-2387-9575.

https://doi.org/10.1016/j.precamres.2020.105857
Received 29 February 2020; Received in revised form 20 May 2020; Accepted 10 July 2020
Available online 15 July 2020
0301-9268/

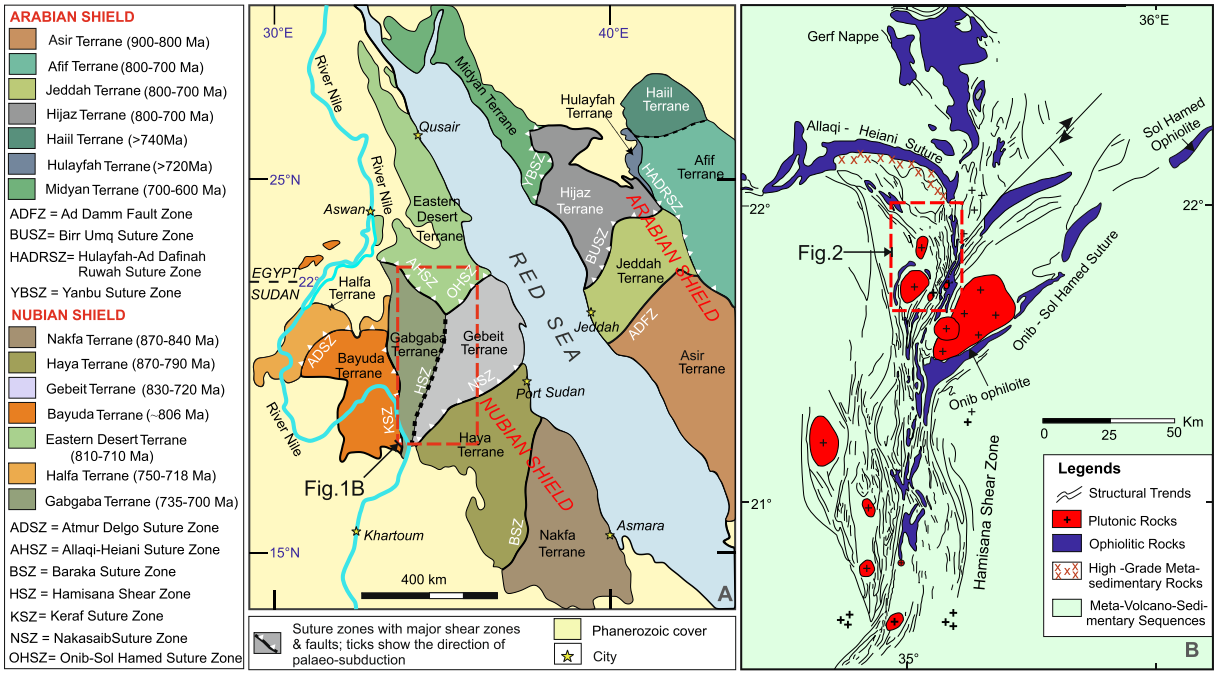

Fig. 1. (A). Structural and metamorphic map of the Arabian-Nubian Shield (Modified after Johnson and Woldehaimanot (2003)), showing tectonostratigraphic terranes, with the estimated terrane protolith ages, and subduction orientations, suture zones, and boundaries between the ANS and flanking older crustal blocks. The dashed-line, red rectangular is the Hamisana Shear Zone (HSZ) marked as B. (B) Generalized map of plexus, including the eastern part of Allaqi-Heiani suture, Gerf nappe, Onib-Sol Hamed suture, and Hamisana shear zone (modified after Stern et al. (1990)). The study area (Fig. 2) is shown by a dashed-lined, red rectangular. (For interpretation of the references to color in this figure legend, the reader is referred to the web version of this article.)

Dilek and Ahmed, 2003). This juvenile crust consists mainly of low- to medium-grade, metamorphosed Neoproterozoic volcanic and sedimentary successions, serpentinites and dismembered ophiolites, metagabbro–diorite–tonalite intrusive complexes, and early calc-alkaline granitoids including monzonite–granodiorite–granite complexes (Stern, 1994). The more evolved calc-alkaline granitoids were emplaced during and after the continental collision episodes but before the onset of large-scale crustal extension in the ANS. Post-collisional (630–590 Ma) extensional deformation within the ANS was accompanied by widespread emplacement of I-type granites, high-K calc-alkaline granitoids, and alkaline A-type intrusions (Johnson et al., 2011), analogous to much younger continental collision zones (Dilek and Whitney, 2000; Dilek, 2006; Altunkaynak et al., 2012). This plutonic episode was coeval with the formation of high-K, shoshonitic volcanic sequences (610–580 Ma), extrusion of mafic to felsic lavas, and deposition of thick clastic sediments in the northern part of the ANS.

The largely juvenile nature of much of the ANS crust and its low metamorphic grade makes the ANS an excellent natural laboratory to investigate the mode, nature and tempo of crustal growth, specifically the timing, melt sources and petrogenesis of widespread granitoid magmatism throughout the East African Orogeny. The Hamisana Shear Zone (HSZ) in NE Sudan and SE Egypt occurs in a critical area within the ANS where several ophiolite-bearing suture zones (i.e., Onib–Sol Hamed and Allaqi–Heinai suture zones) converge, forming a N-NE-trending, lithospheric–scale intra-continental shear zone (Fig. 1). The HSZ has been the focus of much interest and controversy in regard to its signifcance for the East African orogeny and its evolution (Stern et al., 1989, Stern and Kröner, 1993) and because of gold mineralization (Adam et al., in press). Nearly > 60% of the HSZ is composed of granitoids (granite, granodiorite, diorite, quartz syenite and quartz monzonite) and subduction-generated basaltic–andesitic extrusive rocks (Fig. 2; Taylor and McLennan, 1991). However, the petrogenesis of these granitoids, the tectonic environment of the origin of their magmas, and the precise timing of their emplacement are still open questions due largely to a lack of reliable age constraints and viable geochemical and isotopic data (e.g. Wyllie et al. (1976), Wyllie (1984), Chappell et al. (1987), Borg and Clynne (1998), Farahat et al. (2007, 2011), Avigad and Gvirtzman (2009)).

In this study we have investigated the petrology, U-Pb zircon ages, whole-rock geochemistry, and Hf–Sr-Nd isotopic compositions of the Hamisana Shear Zone granitoids (HSZG), the emplacement of which span nearly 40 million years of magmatism during the assembly of the ANS. The HSZ granitoids show a geochemical and geochronological progression through time, and hence the geochemical fingerprints and crystallization ages of their magmas provide important insights into the potential melt sources and the tempo of their melt evolution during juvenile crust development within the central Nubian Shield. In the first part of the paper, we discuss the tectonic history of the ANS and the geology of the HSZ, the field occurrence of the HSZ granitoids, and our analytical methods used in this study. We then present the results of our geochronological, geochemical and isotopic analyses of representative suites of HSZ granitoids. In the last part of the paper, we discuss the timing of the emplacement of the HSZ granitoids, and the petrogenesis and the source of their magmas in a regional tectonic framework. Our data and interpretations provide an important case study for better understanding of juvenile crust formation during the late Proterozoic development of the ANS.

2. Regional geology of the Arabian-Nubian Shield (ANS) and the Hamisana Shear Zone

2.1. Tectonic history of the ANS

The ANS covers a large part in Northeast Africa and West Arabia and includes the largest tract of Neoproterozoic juvenile continental crust in the Earth (Dilek and Ahmed, 2003; Patchett and Chase, 2002; Stern et al., 2004). This juvenile crust was produced when island arc terranes were formed within and around the margins of the Mozambique Ocean, which evolved during the breakup of Supercontinent Rodinia around 800–900 Ma (Stern, 1994; El-Rahman et al., 2009a,b;

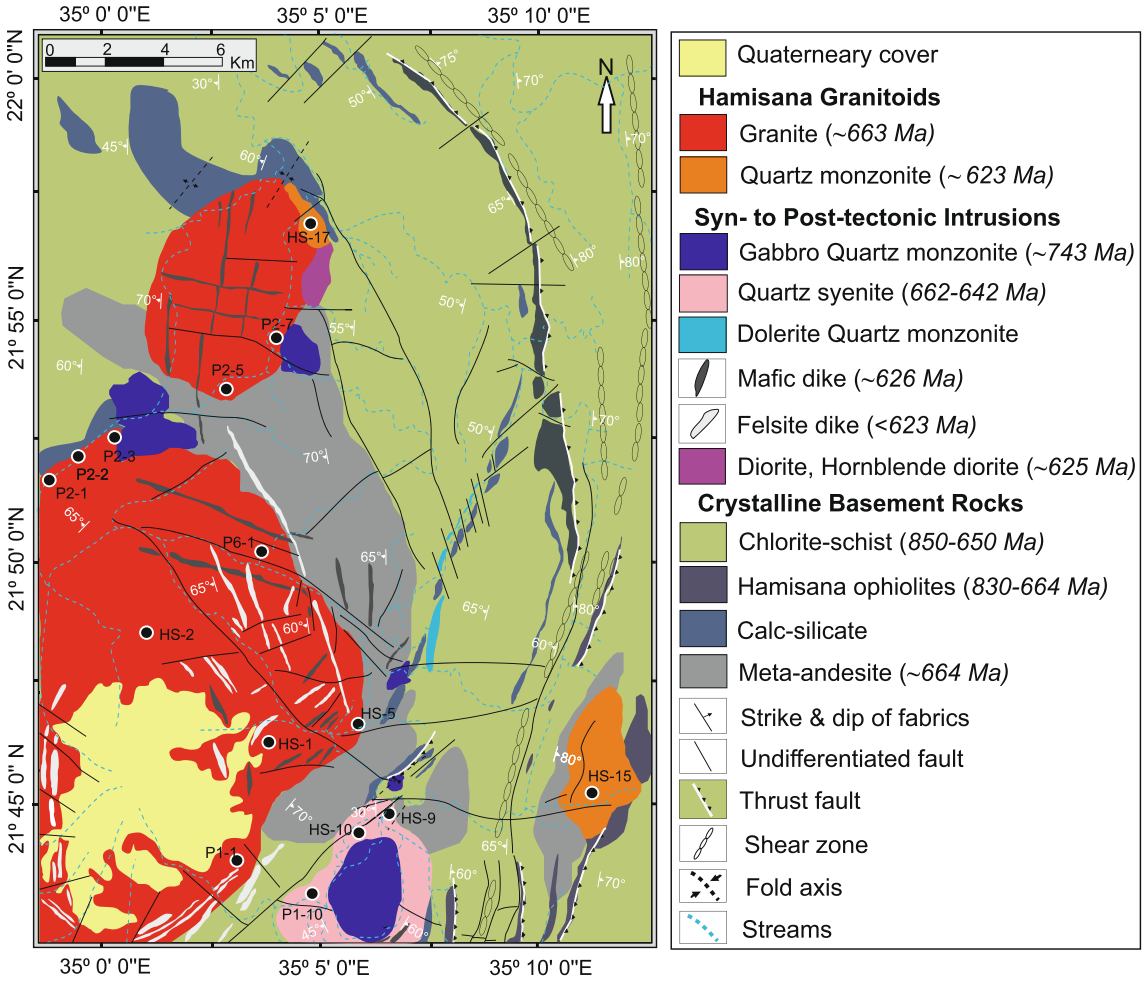

Fig. 2. Geological map of the Northern Hamisana Shear Zone, showing major rock units, structures, and granitoid sample locations. The corresponding ages are based on our unpublished data.

Eliwa et al., 2014). The tectonic evolution of the ANS records ~300 m.y. of crustal growth and orogenic evolution from intra-oceanic subduction, island arc and back-arc magmatism (870–700 Ma), to terrane amalgamation during the closure of the Mozambique Ocean (~800–650 Ma) and finally the terminal collisions between the major lithospheric fragments of East and West Gondwana. The formation of the ANS took place during the closure of the Mozambique Ocean between the East and West Gondwana continental blocks. Ocean closure led to the amalgamation of numerous ca. 870–625 Ma juvenile arc and back-arc igneous and sedimentary rock sequences (Zoheir et al., 2019). This orogenic buildup was followed by the collapse of a thickened and elevated crust of the East African Orogen (EAO), accompanied by tectonic escape, strike-slip faulting, delamination, and extension (630–550 Ma; Avigad and Gvirtzman, 2009; Fritz et al., 2013; Genna et al., 2002; Hargrove et al., 2006a, 2006b; Johnson et al., 2011; Kröner, 1985; Kröner et al., 1987; Meyer et al., 2014; Stern, 1994; Stern and Johnson, 2010; Stoeser and Camp, 1985; Ali et al., 2013; Be'eri-Shlevin et al., 2012; Johnson and Woldehaimanot, 2003, and references therein).

The ANS and the adjacent Mozambique Belt represent one of the most extensive Neoproterozoic metamorphic zones of the Earth. The Mozambique Belt is composed predominantly of amphibolite-facies rocks with extensive tracts of granulites, which are considered to have formed during the collision of East and West Gondwana (Burke et al.,1977; Shackleton, 1986; Stern and Dawoud, 1991). The ANS consists largely of greenschist-facies metamorphic rocks. Therefore, the difference between the ANS and the adjacent Mozambique Belt is in the metamorphic grade of their rock assemblages that resulted from arc-arc versus continent–continent collisions, respectively.

The 400-km wide and 200-km long Najd fault system (Stern et al., 1989) in the ANS is characterized by a cumulative sinistral offset of 240–300 km (Davies, 1984). It was active between 655 and 540 Ma, after the final assembly of the ANS (Stacey and Agar, 1985). In NE Sudan, the N40W-striking Oko shear zone constitutes part of the Najd fault system, and also displays sinistral offsets (Almond and Ahmed, 1987).

Major suture zones of the ANS are classified into two types: arc–arc and arc-continent collision sutures (Fig. 1; Abdelsalam and Stern, 1996). The arc–arc sutures trend mostly NE–SW representing the zones of closure of oceanic basins between juvenile arc terranes at 800–700 Ma (examples include Allaqi-Heiani-Onib-Sol, Hamed-Yanbu and Nakasib-Bir Umq sutures; Fig. 1; Pallister et al., 1988; Kröner et al., 1991; Dilek and Ahmed, 2003; Johnson et al., 2003). Following the arc–arc collisions, the newly assembled ANS collided with two pre-Neoproterozoic continental blocks, East- and West-Gondwana, throughout 750–630 Ma. These collisions are now represented by the N-S trending Nabitah suture zone in the east and the Keraf suture zone in the west (Stern et al., 1989; Stern, 1994; Johnson et al., 2003). Abdelsalam and Stern (1996) refer to these boundaries as arc-continent sutures. The ANS underwent north–south shortening during the final collision of East- and West-Gondwana between 650 and 550 Ma (Abdelsalam and Stern, 1996; Stern et al., 2004).

In northeast Sudan, the Nubian component of the ANS is composed of several arc terranes, which include Gerf, Gabgaba, Gebeit, Haya and

Tokar (Fig. 1). These arc complexes are separated by sutures and the associated shear zones, such as the Hamisana (HSZ), Oko (OSZ) and Nakasib Suture Zones (NSZ; Stern, 1994). The Hamisana shear zone in northern Sudan is a well-known example of a arc-continent suture zone (Fig. 1b), which displays east–west crustal shortening fabrics, steeply plunging folds, and major thrust faults. It represents one of the largest basement structures in NE Africa (Stern, 1989).

2.2. The Hamisana Shear zone

The HSZ is one of the major, Pan-African high-strain zones exposed in northeastern Sudan and southeastern Egypt within the ANS. It is approximately 50-km-wide and ~300-km-long, displaying crustal-scale shortening and strike-slip deformation fabrics (Fig. 1a and b; Vail, 1985). The oldest basement sequences within the HSZ consist of metasedimentary rocks, migmatites, and metavolcanic suites forming schist and gneiss units (Fig. 2). Metavolcanic and metasedimentry rock sequences are dominated by *meta*-andesites and chlorite schist. Others include psammitic and semipelitic schists, with intercalations of calc-silicates, *meta*-arkosic sandstones, and metaquartzites. All these sequences (Bennett and Mosley, 1987; Lissan and Bakheit, 2010) are structurally overlain by dismembered ophiolite nappes and serpentinized peridotites (Gerf nappe of Kröner et al., 1987). The Hamisana ophiolites contain serpentinite, cumulate peridotites, layered and isotropic gabbros, plagiogranite, sheeted dikes, and pillow lavas, typical of subduction–related ophiolite sequences (Dilek et al., 1990; Dilek and Thy, 1998; Dilek and Furnes, 2011, 2014). These metavolcanic and metasedimentry sequences and ophiolitic nappes were folded, and were subsequently intruded extensively by syn- to late-tectonic plutons of gabbro-diorite-tonalite-granite compositions (Fig. 2; Miller and Dixon, 1992). Relatively unmetamorphosed volcanic and pyroclastic rock sequences were widely intruded, especially in the north, by batholithic quartz monzonite and monzonite–granodiorite–granite plutons as well as by mafic and felsic dike swarms (Fig. 2; Stern, 1994).

3. Field occurrence and petrography of the HSZ granitoids

Fifteen granitoid samples from the northern part of the Hamisana Shear Zone in the ANS were used for petrographic investigation and geochemical analysis (Table 1). The selected granitoid samples comprise granite (n = 4), granodiorite (n = 3), quartz syenite (n = 4), and quartz monzonite (n = 4). The locations of these samples shown in (Fig. 1a). According to geochronological results, we classify these granitoids into two groups: the first group includes older granitoids composed of granite, granodiorite and quartz syenite that display extensive shear and deformation fabrics, whereas the younger granitic rocks are composed mainly of quartz monzonite. All granitoids are intruded into metavolcano-sedimentary sequences consisting of *meta*-andesite and chlorite schist (Fig. 2). Chilled margins occur between the granitoid intrusions and their host *meta*-andesites (Fig. 3a, b), and some intrusions contain *meta*-volcanic fragments as xenoliths (Fig. 3c); these features collectively indicate that emplacement of these plutons occurred at shallow crustal levels and long after the eruptions of andesitic lavas.

3.1. HSZ granites and granodiorites

Granites are the predominant igneous rock type located in the SW and NW parts of the study area (Fig. 2). Granodiorite also occurs, although less commonly and with unclear contact relationships with the granitic rocks. Both granites and granodiorites show intense deformation and shear fabrics, defined by foliation and mineral–elongation parallel to the general orientation of shear zones (Fig. 3d–f).

Granitic rocks are commonly grey colored, have a coarse-grained granular texture, and consist mainly of quartz, alkali feldspar, biotite and hornblende. Accessory minerals include titanite, opaque Fe–Ti oxides, allanite, apatite, and zircon. Quartz shows anhedral and wavy extinction. Granulation and recrystallization textures are common along the grain boundaries of both quartz and feldspar. Alkali feldspar grains are anhedral in shape and are locally altered to clay minerals (Fig. 4a, b). Biotite displays subhedral to anhedral habits and incipient foliation (Fig. 4b).

Granodiorite rocks are heterogeneous in texture, varying from coarse- to medium-grained, and with granular to inequigranular porphyritic textures; they are slightly foliated. All granodiorites consist primarily of alkali feldspar, plagioclase, quartz, and biotite with scarce hornblende. Accessory minerals include opaque iron oxides, titanite, allanite, apatite, and zircon (Fig. 4c, d). Plagioclase occurs as subhedral to anhedral, tabular and equant crystals that are commonly polysynthetic, twinned, and chemically zoned, and is generally altered. Vermicular or wormy intergrowth of alkali feldspar into plagioclase grains formed a myrmekititic texture between the two. Alkali feldspar also occurs as subhedral to anhedral, interstitial grains. Inclusions of biotite, hornblende, and plagioclase are locally enclosed within alkali feldspars (Fig. 4c). Quartz is found as both small interstitial and large grains. Larger quartz crystals commonly display a wavy and undulatory extinction, deformation bands, and granulation. Plagioclase and K-feldspar display preferred orientation. Biotite is partly altered to chlorite and opaque minerals, whereas hornblende is replaced by biotite and/or chlorite (Fig. 4c, d).

3.2. Quartz syenite

Quartz *syenite*, located in the southern part of the mapped area (Fig. 2), is intrusive into the metavolcanic and metasedimentary sequences of the ANS, and is in turn intruded by Cretaceous gabbroic dikes and stocks (Fig. 3g, h). The Quartz *syenitic* rocks are characterized by their gray and reddish to pinkish color, and are coarse-grained with porphyritic textures. They consist mainly of alkali feldspar, plagioclase, quartz, and biotite (Fig. 4e, f). Euhedral to subhedral titanite is by far the most abundant (up to 3%) accessory mineral. Other accessory minerals include opaque iron oxides, allanite, apatite, and zircon (Fig. 4e, f). Alkali feldspars are represented by microperthite and homogeneous microcline, and occur as subhedral to anhedral interstitial grains. Quartz occurs as both small interstitial grains and large grains with irregular shapes; it commonly displays undulatory extinction, deformation bands, and granulation along grain boundaries (Fig. 4e). Biotite is altered to chlorite and opaque minerals. Lozenge-shaped titanite and biotite with a well-developed preferred orientation indicate contractional strain during and after their crystallization.

3.3. Quartz monzonite

Quartz monzonitic intrusions occur in the northern and southeastern parts of the study area (Fig. 2) and represent the youngest granitoid suite with no or little deformation (Fig. 3i). The Quartz monzonitic rocks are commonly gray to pink in color and display massive, coarse-grained and granular textures. They consist mainly of plagioclase, alkali feldspar, quartz, and mafic minerals (mainly hornblende and biotite) (Fig. 4g, h). Main accessory minerals include opaque iron oxides, monazite, apatite, and zircon (Table 1; Fig. 4g, h). Plagioclase is the dominant mineral phase (25–35 vol%) and forms euhedral to subhedral lath-shaped crystals, commonly displaying albite, carlsbad, and pericline twinnings. It is locally altered to sericite and/or clay minerals. Quartz occurs (less than 5 wt%) as large interlocked grains (up to 3.5 mm), and locally contains biotite inclusions. Biotite also occurs as independent and coalesced tabular crystals and flakes of variable sizes, and is commonly altered to chlorite and epidote. Muscovite is partially intergrown with biotite (Fig. 4g, h). Inclusions of biotite, hornblende, zircon and apatite occur in feldspar grains. Amphibole (hornblende) locally shows an epitaxial growth texture in biotite grains (Fig. 4h).

Table 1
Whole rock major, trace and rare earth elements of Hamisana granitoids in the Arabian-Nubian Shield.

Sample No.	P2-1	P2-2	P2-3	HS-1	HS-2	P1-1	P6-1	HS-5	HS-10	HS-9	P1-10	HS-15	HS-17	P2-5	P2-7
Rock Name	Granodiorite			Granite				Quartz syenite				Quartz monzonite			
Major elements (wt. %)															
SiO_2	70.1	69.7	68.8	71.73	71.60	72.24	72.52	67.4	66.63	66.23	67.38	60.0	60.3	60.6	61.1
TiO_2	0.28	0.31	0.28	0.36	0.36	0.34	0.36	0.51	0.39	0.45	0.43	1.02	1.01	1.00	1.00
Al_2O_3	16.81	16.94	17.21	14.67	14.90	14.52	14.66	17.01	17.4	17.38	16.9	17.99	17.63	19.32	17.45
Fe_2O_3	1.7	1.7	1.7	1.7	1.7	1.6	1.7	2.0	2.0	1.9	1.9	5.3	5.4	4.7	4.9
MnO	0.02	0.03	0.03	0.04	0.05	0.05	0.04	0.05	0.03	0.03	0.03	0.1	0.1	0.09	0.92
MgO	0.84	0.86	0.85	0.50	0.50	0.48	0.47	0.35	0.21	0.32	0.32	2.46	2.35	1.72	1.99
CaO	2.96	2.87	3.02	1.33	1.34	1.33	1.32	0.85	0.69	0.83	0.75	4.1	4.0	3.44	3.66
Na_2O	4.39	4.45	4.83	4.57	4.50	4.32	4.25	5.18	6.04	5.69	5.78	4.6	4.7	5.03	4.90
K2O	1.9	2.1	2.2	3.87	3.87	3.65	3.60	5.8	5.47	5.23	5.40	3.2	3.1	2.9	3.1
P_2O_5	0.10	0.10	0.10	0.10	0.10	0.09	0.10	0.10	0.10	0.11	0.10	0.50	0.49	0.37	0.37
LOI	0.85	0.99	0.96	1.15	1.13	1.35	1.03	0.75	1.0	1.84	1.0	0.74	1.00	0.83	0.68
Total	99.99	100.00	100.01	99.99	100.00	100.03	100.00	100.00	99.99	100.00	100.03	100.00	100.01	99.99	100.00
FeOt	1.54	1.52	1.52	1.51	1.50	1.48	1.49	1.81	1.78	1.71	1.73	4.8	4.9	4.22	4.39
Na_2O/K_2O	2.3	2.1	2.2	1.2	1.2	1.2	1.2	0.9	1.1	1.1	1.1	1.4	1.5	1.7	1.6
K_2O/Na_2O	0.44	0.47	0.45	0.85	0.86	0.85	0.85	1.11	0.91	0.92	0.93	0.7	0.7	0.57	0.62
Mg#	49.25	50.35	49.94	37.02	37.38	36.45	35.89	25.34	17.41	25.31	24.92	47.8	46.2	42.04	44.66
A/CNK	1.1	1.1	1.1	1.04	1.06	1.08	1.10	1.0	1.02	1.05	1.01	1.0	1.0	1.1	1.0
A/NK	1.81	1.77	1.67	1.25	1.29	1.31	1.35	1.15	1.10	1.16	1.10	1.63	1.60	1.69	1.54
FeOt/MgO	1.84	1.76	1.79	3.03	2.99	3.11	3.18	5.25	8.46	5.26	5.37	1.94	2.08	2.46	2.21
Trace elements (ppm)															
Li	12.73	13.23	12.40	8.4	8.6	8.5	8.7	8.2	6.6	7.3	6.8	15.4	15.2	14.5	14.3
Be	1.1	1.2	1.1	2.1	2.2	2.2	2.2	2.6	2.9	2.8	2.8	2.36	2.30	2.36	2.34
Sc	4.42	4.37	4.40	3.55	3.55	3.53	3.54	9.71	10.39	9.82	10.19	9.25	9.17	6.93	6.97
V	30.56	29.43	30.53	21.21	20.46	21.61	20.86	20.04	18.00	19.19	18.50	99.63	98.23	76.96	76.86
Cr	8.34	7.98	8.31	1.89	1.91	1.92	1.90	1.09	1.13	1.12	1.10	28.53	28.33	26.85	23.99
Co	124.24	121.24	123.24	105.65	105.16	104.75	106.16	69.22	44.86	45.82	46.46	58.74	57.14	33.84	37.84
Ni	4.43	4.30	4.41	2.73	2.80	2.76	2.83	1.09	1.12	1.10	1.12	19.50	17.60	5.00	5.14
Cu	1.25	1.19	1.23	1.41	1.41	1.42	1.41	1.74	1.56	1.66	1.89	10.36	10.16	5.99	6.19
Zn	41.63	40.43	41.69	43.9	43.7	43.8	43.6	20.4	16.7	17.6	18.9	77.6	77.0	76.5	76.4
Ga	20.7	19.5	20.3	19.7	19.4	19.6	19.5	19.2	22.4	20.5	22.3	22.57	22.47	23.20	22.80
Rb	39.08	38.28	39.48	44.31	43.67	44.41	43.64	34.52	31.08	30.42	32.28	78.74	78.44	81.72	84.12
Sr	413.90	409.90	411.90	332.31	327.33	334.31	329.33	494.94	572.02	564.94	561.02	1134.93	1128.93	917.11	928.11
Zr	114.96	107.96	112.96	261.62	259.98	260.62	260.12	917.40	1031.86	1029.40	1027.86	246.07	242.07	232.06	238.06
Nb	2.27	2.29	2.28	9.48	9.35	9.45	9.36	11.58	13.87	12.98	13.57	12.09	11.69	13.67	13.27
Mo	0.08	0.08	0.08	0.32	0.30	0.31	0.31	0.92	1.02	0.95	1.01	0.93	0.91	0.44	0.45
Sn	1.06	1.07	1.05	1.21	1.23	1.23	1.22	1.08	1.21	1.18	1.19	1.45	1.43	1.34	1.33
Cs	0.83	0.88	0.84	0.46	0.47	0.47	0.48	0.71	0.33	0.40	0.38	2.22	2.21	1.33	1.32
Ba	473.52	461.52	470.52	744.48	722.41	741.48	726.41	1040.94	1217.51	1182.94	1217.51	925.83	921.83	936.89	1018.89
Hf	3.20	3.21	3.21	6.27	6.19	6.27	6.19	13.58	16.81	15.58	16.21	5.62	5.61	5.58	5.54
Ta	0.47	0.46	0.48	0.7	0.7	0.7	0.7	1.0	1.0	1.0	1.0	0.9	0.8	1.0	0.9
Ti	0.3	0.3	0.3	0.3	0.4	0.3	0.4	0.3	0.2	0.3	0.2	0.50	0.47	0.42	0.40
Pb	10.21	10.26	10.26	17.76	17.49	17.86	17.59	27.62	22.56	23.12	22.86	12.35	12.05	11.30	11.20
Th	5.02	5.21	4.98	4.59	4.63	4.60	4.62	6.00	4.86	5.02	4.96	4.53	4.43	4.74	4.62
U	1.00	1.03	1.02	1.03	1.06	1.03	1.05	1.99	2.20	2.14	2.17	1.61	1.54	1.47	1.45
La	14.41	13.81	14.56	39.99	39.86	39.59	39.76	41.97	38.34	40.77	39.36	36.74	36.44	32.86	30.76
Ce	28.57	27.87	28.27	80.13	78.82	80.03	78.92	90.13	84.95	86.17	84.95	86.60	86.30	69.10	68.55
Pr	3.21	3.19	3.20	8.61	8.43	8.59	8.45	10.47	9.85	11.96	9.85	10.44	10.04	9.34	9.29
Nd	11.95	12.05	12.55	30.07	29.84	30.05	29.85	38.96	35.51	36.36	34.81	41.58	40.28	26.45	26.25
Sm	2.12	2.09	2.10	4.55	4.60	4.58	4.59	6.19	4.95	5.19	4.98	7.12	7.02	4.92	4.91
Eu	0.59	0.55	0.60	1.16	1.06	1.14	1.09	1.98	1.47	1.51	1.46	2.06	2.04	2.17	2.16
Gd	1.48	1.47	1.49	3.1	3.1	3.1	3.1	3.9	2.8	2.9	2.8	5.0	4.5	4.2	4.1
Tb	0.2	0.2	0.2	0.4	0.4	0.4	0.4	0.5	0.4	0.4	0.4	0.64	0.61	0.58	0.56
Dy	0.89	0.85	0.87	2.31	2.22	2.30	2.24	2.12	2.04	2.09	2.06	3.30	3.23	3.07	3.05
Ho	0.16	0.17	0.18	0.43	0.41	0.42	0.40	0.47	0.43	0.44	0.45	0.58	0.57	0.58	0.56
Er	0.41	0.42	0.40	1.12	1.07	1.11	1.09	1.38	1.33	1.36	1.35	1.56	1.54	1.66	1.64
Tm	0.05	0.06	0.06	0.16	0.17	0.17	0.16	0.22	0.23	0.21	0.22	0.21	0.22	0.25	0.23
Yb	0.35	0.34	0.37	1.07	1.09	1.07	1.09	1.64	1.80	1.78	1.81	1.39	1.38	1.60	1.55
Lu	0.05	0.05	0.05	0.16	0.16	0.16	0.16	0.30	0.32	0.31	0.32	0.22	0.21	0.24	0.25
Y	4.8	4.3	4.6	13.0	12.6	13.1	12.7	13.8	12.8	13.3	13.0	17.14	16.74	17.45	17.35
ΣREE	69.2	67.6	69.5	186.3	183.9	185.9	184.0	214.1	197.2	204.8	197.8	214.57	211.09	174.43	171.25
(La)N	39.26	37.63	39.68	108.97	108.60	107.88	108.33	114.35	104.47	111.08	107.25	100.11	99.30	89.55	83.83
(Yb)N	1.41	1.37	1.49	4.31	4.39	4.31	4.38	6.63	7.26	7.20	7.30	5.61	5.57	6.44	6.24
(La/Yb)N	27.77	27.39	26.55	25.30	24.71	25.05	24.74	17.25	14.40	15.44	14.70	17.84	17.82	13.91	13.44
(Ce)n	29.86	29.12	29.54	83.73	82.36	83.62	82.46	94.17	88.76	90.04	88.76	90.49	90.18	72.21	71.63
(Ce/Yb)n	21.11	21.20	19.77	19.44	18.74	19.42	18.83	14.20	12.23	12.51	12.17	16.13	16.19	11.21	11.48
(Sm)n	9.17	9.04	9.08	19.68	19.91	19.81	19.87	26.78	21.44	22.46	21.57	30.83	30.40	21.29	21.25
(La/Sm)n	4.28	4.16	4.37	5.54	5.45	5.45	5.45	4.27	4.87	4.95	4.97	3.25	3.27	4.21	3.95
(Gd)n	4.82	4.81	4.85	10.09	10.06	10.13	10.11	12.90	9.23	9.57	9.30	16.28	14.58	13.61	13.54

(*continued on next page*)

Table 1 (*continued*)

Sample No.	P2-1	P2-2	P2-3	HS-1	HS-2	P1-1	P6-1	HS-5	HS-10	HS-9	P1-10	HS-15	HS-17	P2-5	P2-7
Rock Name	Granodiorite			Granite				Quartz syenite				Quartz monzonite			
(Gd/Yb)n	3.41	3.50	3.25	2.34	2.29	2.35	2.31	1.95	1.27	1.33	1.27	2.90	2.62	2.11	2.17

FeOT: $Fe_2O_3T \times 0.8998$; LOI: loss on ignition; Mg#: (100MgO/(MgO + FeO); A/CNK = $Al_2O_3/(CaO + Na_2O + K_2O)$; A/NK = $Al_2O_3/(Na_2O + K_2O)$; ΣREE = Sum of Rare Earth Elements; (La)N, (Yb)N, (La/Yb)N, Ce)n, (Ce/Yb)n, (Sm)n, (La/Sm)n, (Gd)n, (Gd/Yb)n = are chonderite-normalized values from (McDonough and Sun (1995)). Major elements in wt %; trace elements in ppm.

4. Analytical methods

4.1. LA-ICP-MS zircon U-Pb dating

Magnetic and conventional heavy liquid techniques were used in zircon separation. This process was followed by handpicking under a binocular microscope to separate the zircon grains from fresh granitoids samples. The selected zircons were examined under transmitted and reflected light with an optical microscope, and cathodoluminescence (CL) images were collected on a CAMECA SX51 under conditions of 50 kV and 15nA at Wuhan Sample Solution Analytical Technology Co., Ltd., Wuhan, China. The CL images were used to examine the internal textures and to choose potential targets for U–Pb dating and Lu-Hf isotope analysis.

U-Pb dating and trace element analyses of separated zircons were conducted in the State Key Laboratory of Geological Processes and Mineral Resources (GPMR), China University of Geosciences-Wuhan, China. Experiments were performed on an Agilent 7500a ICP-MS instrument (Agilent Technology, Tokyo, Japan) in combination with an ArF excimer laser (λ = 193 nm) (GeoLas 2005, MicroLas, Göttingen, Germany). The operating conditions for the LA-ICP-MS instrument were similar to Liu et al. (2010a, b). All analyses were performed with a laser spot size of 32 μm, a repetition rate of 5 Hz, and a fluence of 8 J/cm^2 in this study. Helium was used as the carrier gas in the ablation cell and merged with argon (makeup gas) behind the ablation cell (Günther and Heinrich, 1999; Luo et al., 2018a). A signal-smoothing and mercury-removing device was used in this laser ablation system to obtain smooth signals and reduce the mercury signal (Hu et al., 2014). A small amount of (4.1 mg min^{-1}) water vapor was added before the ablation cell to improve the analytical accuracy and precision (Luo et al., 2018b). Each single-spot analysis consisted of 20 s of background signal acquisition, followed by 50 s of ablation. Zircon 91,500 (Wiedenbeck et al., 1995)

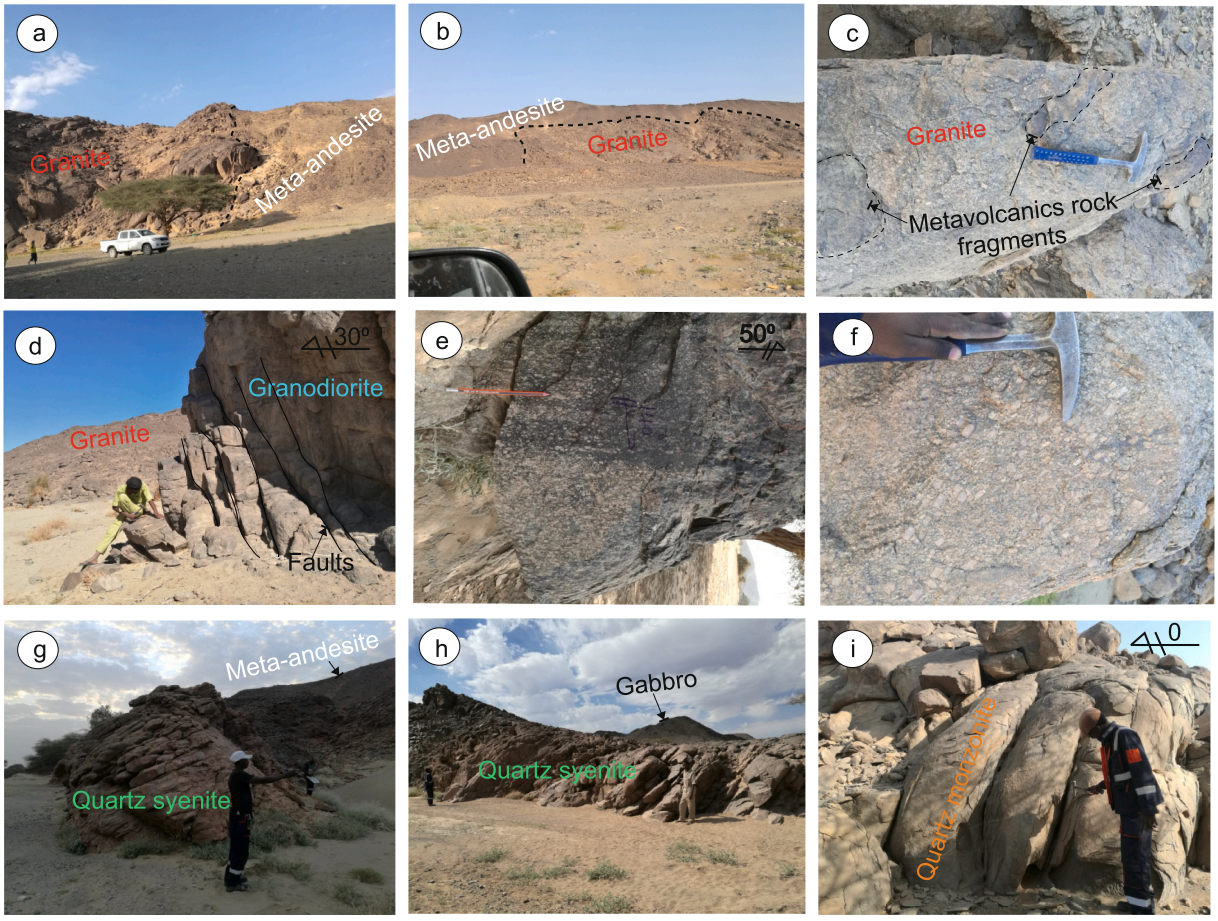

Fig. 3. (a) Field photos of a post-collisional quartz monzonite intrusion, characterized by an ex-foliation weathering in large, undeformed boulders; (b) a faulted granodiorite with a granitic rock in the background; (c) Syntectonic quartz syenite intruded into *meta*-andesite and chlorite schist, displaying foliation with NWW strike and a gentle dip (20–35) to the south; (d) intrusive gabbroic rock; (e and f) contact relationships between granite and *meta*-andesite; (g and h) foliation and mineral elongation lineation in syntectonic granitoids parallel to the shearing orientation, mainly vertical to sub-vertical NE and NW directions; (i) metavolcanic rock xenoliths in granite near the contact.

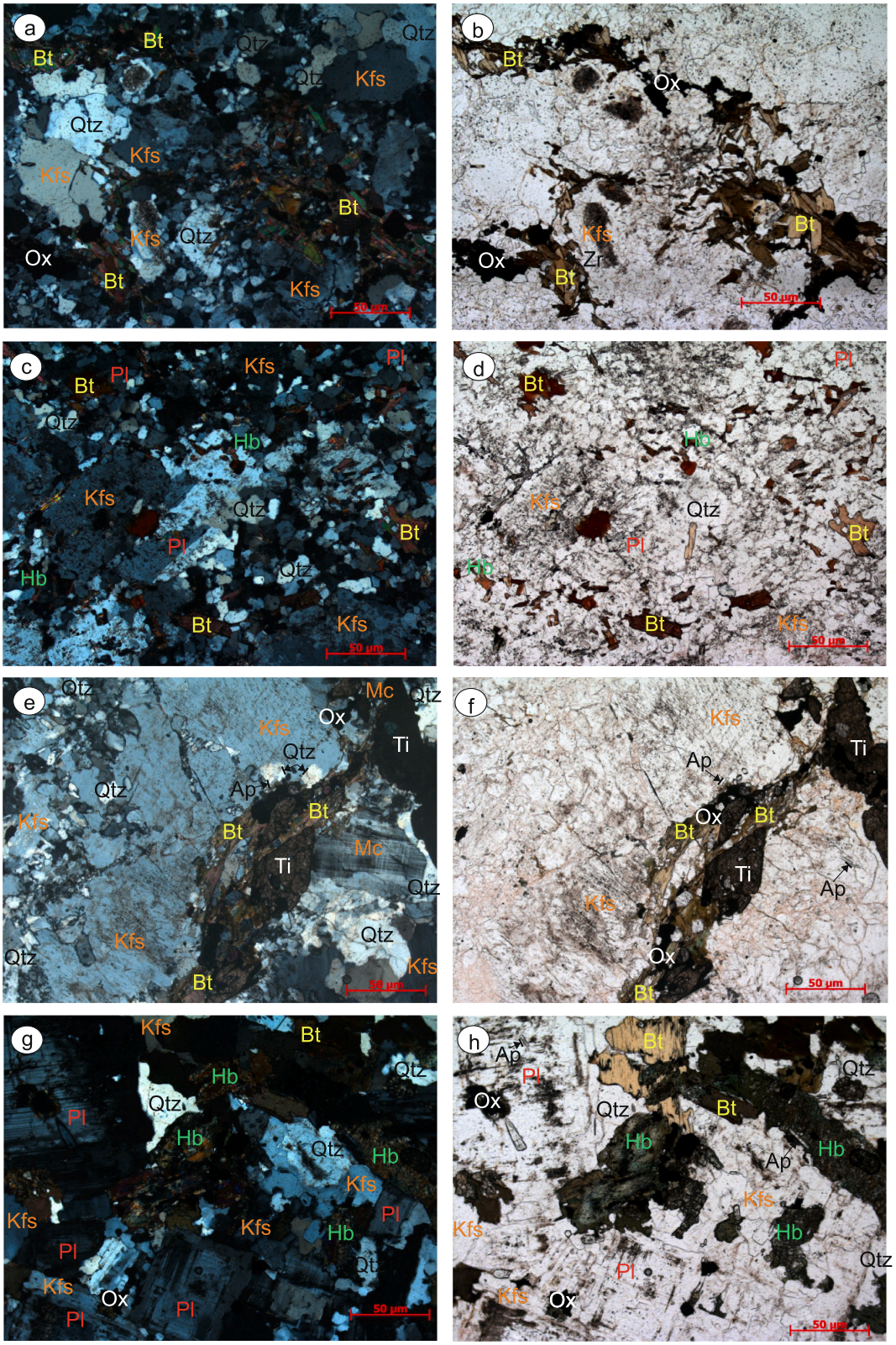

Fig. 4. (a and b) Photomicrographs and reflected light images showing mineral assemblages and textures in a Northern HSZ granite; (c and d) granodiorite; (e and f) quartz syenite; (g and h) quartz monzonite, in both XPL and PPL, respectively. Qtz = Quartz; Bt = Biotite; Pl = Plagioclase; Hb = Hornblende; Kfs = K-feldspar; Mc = Muscovite; Ox = Iron oxide; Ti = Titanite; Zr = Zircon; and Ap = Apatite.

was used as an external standard to correct the Pb/U fractionation and instrumental mass discrimination, and zircon GJ-1was analyzed as an unknown. The obtained weighted average $^{206}Pb/^{238}U$ ages in 12 analyses of GJ-1 is 606.4 ± 4.1 Ma in this study, which are consistent with the reference age of 599.8 ± 1.7 Ma (Jackson et al., 2004). The trace element compositions of zircons were calibrated against NIST 610 glass as an external calibration and combined with ^{29}Si as internal standardization (Liu et al., 2010b). Off-line selection and integration of

Table 2
LA-ICP-MS zircon U-Pb data of the Hamisana granitoids in the Arabian-Nubian Shield.

Elements contents (ppm)					Isotopic ratios									Apparent age (Ma)							
Spot	Pb total	Th232	U238	Pb*	$^{207}Pb/^{206}Pb$	1sigma	$^{207}Pb/^{235}U$	1sigma	$^{206}Pb/^{238}U$	1sigma	$^{208}Pb/^{232}Th$	1sigma	$^{238}U/^{232}Th$	$^{207}Pb/^{206}Pb$	1sigma	$^{207}Pb/^{235}U$	1sigma	$^{206}Pb/^{238}U$	1sigma	$^{208}Pb/^{232}Th$	1sigma
HS-1 Granite																					
1	82	160	124	36.5	0.0594	0.0019	0.8928	0.0277	0.1089	0.0012	0.0333	0.0008	0.8282	589	73.1	648	14.9	667	7.0	662	15.6
2	83	141	237	0.00	0.0622	0.0017	0.9320	0.0255	0.1087	0.0012	0.0344	0.0009	1.7687	681	59.3	669	13.4	665	6.8	683	17.3
3	72	137	122	13.8	0.0608	0.0023	0.8984	0.0320	0.1082	0.0016	0.0340	0.0009	0.9807	633	86.1	651	17.1	662	9.3	676	16.8
4	26.4	42.1	68.2	17.1	0.0693	0.0029	0.9541	0.0377	0.1094	0.0015	0.0362	0.0013	1.7281	906	85.2	731	23.1	668	8.4	718	26.2
5	24.1	39.3	60.6	0.00	0.0589	0.0027	0.8806	0.0408	0.1094	0.0018	0.0365	0.0011	1.6474	565	100.0	641	22.0	667	9.4	725	21.1
6	57.1	105	133	0.00	0.0655	0.0021	0.9754	0.0304	0.1088	0.0015	0.0329	0.0008	1.3614	791	68.5	691	15.7	666	8.5	654	15.6
7	276	503	447	0.00	0.0607	0.0023	0.9315	0.0311	0.1092	0.0015	0.0353	0.0007	0.9395	628	53.5	658	11.1	664	8.1	701	14.3
8	50.7	86.3	119	0.00	0.0607	0.0021	0.9084	0.0305	0.1098	0.0018	0.0354	0.0010	1.4706	628	75.9	656	16.2	667	9.8	702	19.4
9	55.8	99.5	123	2.51	0.0628	0.0020	0.9447	0.0303	0.1096	0.0015	0.0342	0.0008	1.3111	702	68.5	671	15.8	669	8.6	679	16.5
10	96	173	149	62.6	0.0604	0.0020	0.9066	0.0309	0.1089	0.0016	0.0352	0.0009	0.9299	620	76.8	655	16.5	666	9.2	699	17.5
11	28.6	54.4	68.4	8.38	0.0609	0.0027	0.9066	0.0387	0.1092	0.0018	0.0313	0.0011	1.4070	639	94.4	655	20.6	668	10.1	623	21.6
12	44.8	81.8	94.0	22.9	0.0631	0.0027	0.9399	0.0371	0.1095	0.0016	0.0338	0.0010	1.3367	722	88.9	673	19.4	669	9.1	671	19.1
13	54.3	101	104	17.2	0.0684	0.0024	0.9493	0.0364	0.1068	0.0014	0.0349	0.0011	1.1276	880	72.2	708	18.4	657	8.0	694	20.9
14	37.2	63.2	97.5	18.4	0.0619	0.0021	0.9220	0.0303	0.1086	0.0014	0.0350	0.0010	1.6717	670	74.1	663	16.0	664	8.3	696	20.2
15	85	157	173	8.19	0.0635	0.0018	0.9312	0.0266	0.1064	0.0012	0.0335	0.0008	1.1640	724	61.1	668	14.0	660	7.3	666	16.4
16	76	134	152	31.3	0.0563	0.0019	0.8688	0.0282	0.1092	0.0013	0.0348	0.0009	1.2221	465	75.9	624	15.5	669	7.4	690	17.1
17	92	174	140	76.5	0.0593	0.0019	0.8799	0.0284	0.1076	0.0014	0.0336	0.0008	0.8439	576	75.0	641	15.4	659	8.3	669	14.7
18	63	127	89.7	30.2	0.0605	0.0023	0.8954	0.0369	0.1071	0.0016	0.0329	0.0010	0.8232	620	50.9	649	19.8	656	9.1	654	19.3
19	41.4	75.5	89.7	6.15	0.0605	0.0024	0.8822	0.0332	0.1075	0.0018	0.0334	0.0010	1.2306	633	52.8	649	17.9	657	9.0	664	18.8
HS-5 Quartz syenite																					
1	24.8	41.3	69.1	0.00	0.0644	0.0026	0.9206	0.0394	0.1079	0.0018	0.0362	0.0013	1.7776	754	87.0	678	20.5	660	10.7	718	25.4
2	74	142	125	0.00	0.0605	0.0021	0.8887	0.0299	0.1072	0.0017	0.0344	0.0009	0.9359	633	74.1	646	16.1	661	10.1	683	18.4
3	19.8	36.2	43.5	0.00	0.0662	0.0034	0.9347	0.0494	0.1094	0.0020	0.0348	0.0012	1.2902	813	109	696	25.3	669	11.8	691	23.4
4	30.6	58.3	51.6	0.00	0.0645	0.0032	0.9115	0.0487	0.1094	0.0018	0.0354	0.0013	0.9471	759	103	689	25.1	669	10.2	702	24.4
5	66	125	93.0	0.00	0.0643	0.0026	0.9484	0.0343	0.1092	0.0020	0.0368	0.0012	0.8034	750	86.3	677	17.9	668	11.4	731	23.5
6	29.9	53.0	70.3	26.7	0.0598	0.0027	0.8896	0.0381	0.1078	0.0019	0.0353	0.0012	1.4223	594	102.8	641	20.6	660	11.1	700	24.2
7	46.7	86.2	86.2	2.72	0.0644	0.0027	0.9494	0.0389	0.1074	0.0018	0.0362	0.0012	1.0764	755	87.8	678	20.3	660	10.3	719	23.0
8	19.6	34.3	51.8	23.8	0.0640	0.0034	0.9278	0.0475	0.1070	0.0020	0.0337	0.0015	1.6140	743	112	666	25.0	658	10.7	671	30.1
9	30.9	56.6	57.0	0.00	0.0637	0.0029	0.9308	0.0442	0.1079	0.0015	0.0348	0.0013	1.0741	731	100.9	679	23.0	660	8.9	691	26.0
10	24.3	45.8	60.3	0.00	0.0639	0.0031	0.9530	0.0461	0.1095	0.0017	0.0317	0.0016	1.4072	739	103	680	24.0	670	9.7	630	30.9
11	39.6	78.4	62.8	0.00	0.0589	0.0032	0.9031	0.0503	0.1081	0.0018	0.0324	0.0018	0.8671	565	119	637	27.3	662	10.5	645	35.8
12	28.2	46.8	64.5	33.1	0.0578	0.0039	0.8912	0.0573	0.1075	0.0016	0.0347	0.0025	1.4761	520	146	620	31.6	658	9.4	690	48.2
13	26.7	50.4	56.3	0.84	0.0591	0.0044	0.9119	0.0669	0.1089	0.0017	0.0308	0.0025	1.1826	569	163	637	36.3	666	10.1	614	49.7
14	37.3	72.2	63.1	0.00	0.0564	0.0047	0.8845	0.0525	0.1078	0.0018	0.0304	0.0029	0.9197	478	186	611	40.4	660	10.6	605	56.5
15	36.5	74.4	55.2	0.00	0.0569	0.0053	0.8989	0.0606	0.1079	0.0018	0.0288	0.0031	0.7811	500	204	613	44.8	660	10.3	573	60.6
16	40.8	78.1	61.9	0.00	0.0558	0.0057	0.8866	0.0682	0.1072	0.0019	0.0299	0.0037	0.8315	443	228	601	49.6	657	11.0	596	71.8
17	245	496	223	42.1	0.0517	0.0056	0.8943	0.0692	0.1084	0.0016	0.0293	0.0040	0.4699	333	50.9	577	51.3	663	9.1	584	78.9
18	22.8	39.3	56.1	0.00	0.0572	0.0061	0.9000	0.0622	0.1073	0.0018	0.0298	0.0039	1.4953	498	232	608	51.5	658	10.5	594	77.2
19	13.1	24.5	31.1	0.00	0.0601	0.0061	0.8866	0.0588	0.1073	0.0020	0.0291	0.0033	1.3422	609	220	634	48.3	659	11.2	580	64.5
HS-15 Quartz monzonite																					
1	51.9	95.7	161	0.00	0.0604	0.0018	0.8442	0.0263	0.1012	0.0014	0.0316	0.0009	1.8023	617	64.8	621	14.5	622	8.3	629	18.1
2	134	270	253	0.00	0.0599	0.0016	0.8414	0.0230	0.1020	0.0013	0.0321	0.0007	1.0966	611	59.2	620	12.7	626	7.6	638	14.0
3	117	236	242	7.87	0.0602	0.0016	0.8376	0.0220	0.1010	0.0012	0.0315	0.0007	1.0859	609	91.7	618	12.2	621	7.0	627	13.6
4	95	200	202	2.50	0.0607	0.0016	0.8452	0.0222	0.1013	0.0011	0.0301	0.0007	1.0599	628	57.4	622	12.2	622	6.5	599	13.6
5	33.0	63.8	85.4	39.9	0.0607	0.0024	0.8477	0.0329	0.1021	0.0014	0.0306	0.0009	1.4699	628	91.7	623	18.1	626	8.2	609	18.6
6	27.9	49.2	98.3	0.00	0.0594	0.0024	0.8248	0.0327	0.1011	0.0014	0.0321	0.0010	2.0978	583	119	611	18.2	621	8.3	638	19.5
7	122	254	239	0.00	0.0624	0.0017	0.8661	0.0240	0.1011	0.0014	0.0309	0.0008	1.0164	700	59.3	633	13.1	621	8.0	616	15.0
8	44.3	86.0	104	12.6	0.0631	0.0026	0.8687	0.0339	0.1015	0.0015	0.0318	0.0009	1.2655	722	88.9	635	18.4	623	8.7	633	18.2
9	156	311	289	32.8	0.0601	0.0017	0.8435	0.0238	0.1019	0.0012	0.0323	0.0007	0.9578	609	93.5	621	13.1	625	6.9	643	14.5
10	114	231	220	0.00	0.0622	0.0017	0.8693	0.0237	0.1019	0.0014	0.0317	0.0008	0.9906	680	55.6	635	12.9	626	8.5	630	15.4

(*continued on next page*)

Table 2 (*continued*)

Elements contents (ppm)					Isotopic ratios									Apparent age (Ma)							
Spot	Pb total	Th232	U238	Pb*	$^{207}Pb/^{206}Pb$	1sigma	$^{207}Pb/^{235}U$	1sigma	$^{206}Pb/^{238}U$	1sigma	$^{208}Pb/^{232}Th$	1sigma	$^{238}U/^{232}Th$	$^{207}Pb/^{206}Pb$	1sigma	$^{207}Pb/^{235}U$	1sigma	$^{206}Pb/^{238}U$	1sigma	$^{208}Pb/^{232}Th$	1sigma
11	49.0	92.1	114	16.0	0.0623	0.0021	0.8682	0.0274	0.1018	0.0015	0.0327	0.0009	1.2859	687	76.8	635	14.9	625	8.9	651	17.6
12	108	218	206	27.3	0.0602	0.0017	0.8390	0.0207	0.1021	0.0014	0.0315	0.0007	1.0320	613	91.7	619	11.4	627	8.3	626	14.1
13	134	259	264	0.00	0.0601	0.0016	0.8484	0.0229	0.1027	0.0014	0.0330	0.0007	1.0401	606	57.4	624	12.6	630	8.4	656	14.6
14	74	143	179	8.31	0.0588	0.0018	0.8210	0.0245	0.1016	0.0015	0.0319	0.0007	1.2634	561	66.7	609	13.7	624	8.9	634	14.0
15	62.6	116	146	20.5	0.0586	0.0019	0.8183	0.0273	0.1015	0.0015	0.0333	0.0010	1.2778	550	70.4	607	15.2	623	8.6	661	18.7
16	38.6	77.7	98.7	16.9	0.0571	0.0025	0.8054	0.0347	0.1003	0.0015	0.0300	0.0009	1.2850	494	98.1	589	19.7	616	8.8	598	17.2
17	87	164	209	5.86	0.0610	0.0018	0.8454	0.0245	0.1005	0.0014	0.0328	0.0009	1.2840	643	63.0	622	13.5	618	8.5	653	18.1
18	60.4	112	141	0.00	0.0601	0.0022	0.8400	0.0303	0.1018	0.0016	0.0332	0.0009	1.2656	606	79.6	619	16.7	625	9.1	659	18.1
19	58.1	110	137	2.55	0.0613	0.0020	0.8517	0.0266	0.1017	0.0018	0.0323	0.0010	1.2640	650	65.7	626	14.6	625	10.6	643	19.2
20	21.4	35.7	76.6	0.00	0.0569	0.0027	0.8102	0.0347	0.1018	0.0018	0.0336	0.0012	2.2157	487	99.1	591	20.8	625	10.7	668	24.0
HS-17 Quartz monzonite																					
1	111	201	372	0.00	0.0594	0.0014	0.8310	0.0189	0.1012	0.0010	0.0303	0.0007	1.8474	583	53.7	614	10.5	622	5.7	603	13.8
2	156	261	427	0.00	0.0602	0.0014	0.9055	0.0216	0.1089	0.0015	0.0336	0.0008	1.6626	609	47.2	655	11.5	666	8.5	668	15.6
3	29.5	47.5	140	0.00	0.0600	0.0020	0.8373	0.0268	0.1012	0.0013	0.0296	0.0009	2.9459	606	72.2	618	14.8	621	7.8	590	18.4
4	270	456	897	0.00	0.0605	0.0013	0.9080	0.0203	0.1085	0.0014	0.0328	0.0008	2.0426	622	80.5	656	10.8	664	8.2	653	15.1
5	80.4	108	465	8.02	0.0591	0.0015	0.8299	0.0204	0.1016	0.0011	0.0310	0.0008	4.2198	572	51.7	614	11.3	624	6.5	616	16.6
6	107	173	411	22.6	0.0618	0.0016	0.8908	0.0227	0.1045	0.0014	0.0312	0.0008	2.3414	733	57.4	647	12.2	641	8.1	621	16.4
7	105	192	352	5.06	0.0603	0.0017	0.8504	0.0238	0.1018	0.0013	0.0289	0.0008	1.8179	613	59.2	625	13.1	625	7.8	575	16.5
8	471	655	1955	22.6	0.0591	0.0014	0.9193	0.0222	0.1127	0.0017	0.0337	0.0009	2.9625	569	58.3	662	11.8	689	9.6	669	17.0
9	123	198	396	23.6	0.0600	0.0016	0.8914	0.0234	0.1076	0.0015	0.0332	0.0009	1.9932	611	55.5	647	12.6	659	8.9	661	17.7
10	31.8	46.1	153	2.60	0.0610	0.0022	0.8956	0.0307	0.1070	0.0016	0.0313	0.0011	3.3368	639	77.8	649	16.5	655	9.3	624	21.8
11	93	121	536	13.7	0.0600	0.0015	0.8420	0.0198	0.1018	0.0014	0.0325	0.0009	4.4893	606	52.6	620	10.9	625	8.2	647	17.8
12	229	324	969	12.7	0.0616	0.0012	0.9266	0.0186	0.1088	0.0014	0.0346	0.0008	3.0335	661	42.6	666	9.8	666	7.9	688	15.6
13	212	402	583	1.17	0.0599	0.0013	0.8448	0.0177	0.1021	0.0011	0.0304	0.0006	1.5253	611	50.9	622	9.7	626	6.7	605	12.7
14	85	150	276	4.94	0.0605	0.0016	0.8557	0.0221	0.1023	0.0012	0.0318	0.0007	1.9271	633	57.4	628	12.1	628	6.9	633	14.5
15	47.2	65.5	205	2.43	0.0618	0.0018	0.8752	0.0251	0.1026	0.0013	0.0379	0.0050	3.2512	733	61.1	638	13.6	630	7.8	752	97.2
16	306	536	1027	47.3	0.0607	0.0013	0.8910	0.0185	0.1060	0.0012	0.0322	0.0007	2.0145	628	44.4	647	9.9	650	6.7	640	14.3
17	62.4	98.9	236	0.00	0.0595	0.0016	0.9145	0.0252	0.1113	0.0015	0.0336	0.0010	2.4885	583	59.3	659	13.4	680	8.4	668	19.8
18	106	180	345	5.94	0.0620	0.0017	0.9193	0.0242	0.1080	0.0015	0.0341	0.0009	2.0078	676	57.4	662	12.8	661	9.0	677	17.9
19	48.9	83.8	188	0.00	0.0603	0.0017	0.8455	0.0245	0.1017	0.0014	0.0323	0.0010	2.3660	617	61.1	622	13.5	624	8.5	642	18.8
20	35.1	48.0	200	0.00	0.0621	0.0017	0.8628	0.0240	0.1010	0.0015	0.0342	0.0012	4.3592	676	58.2	632	13.1	620	8.8	679	22.8

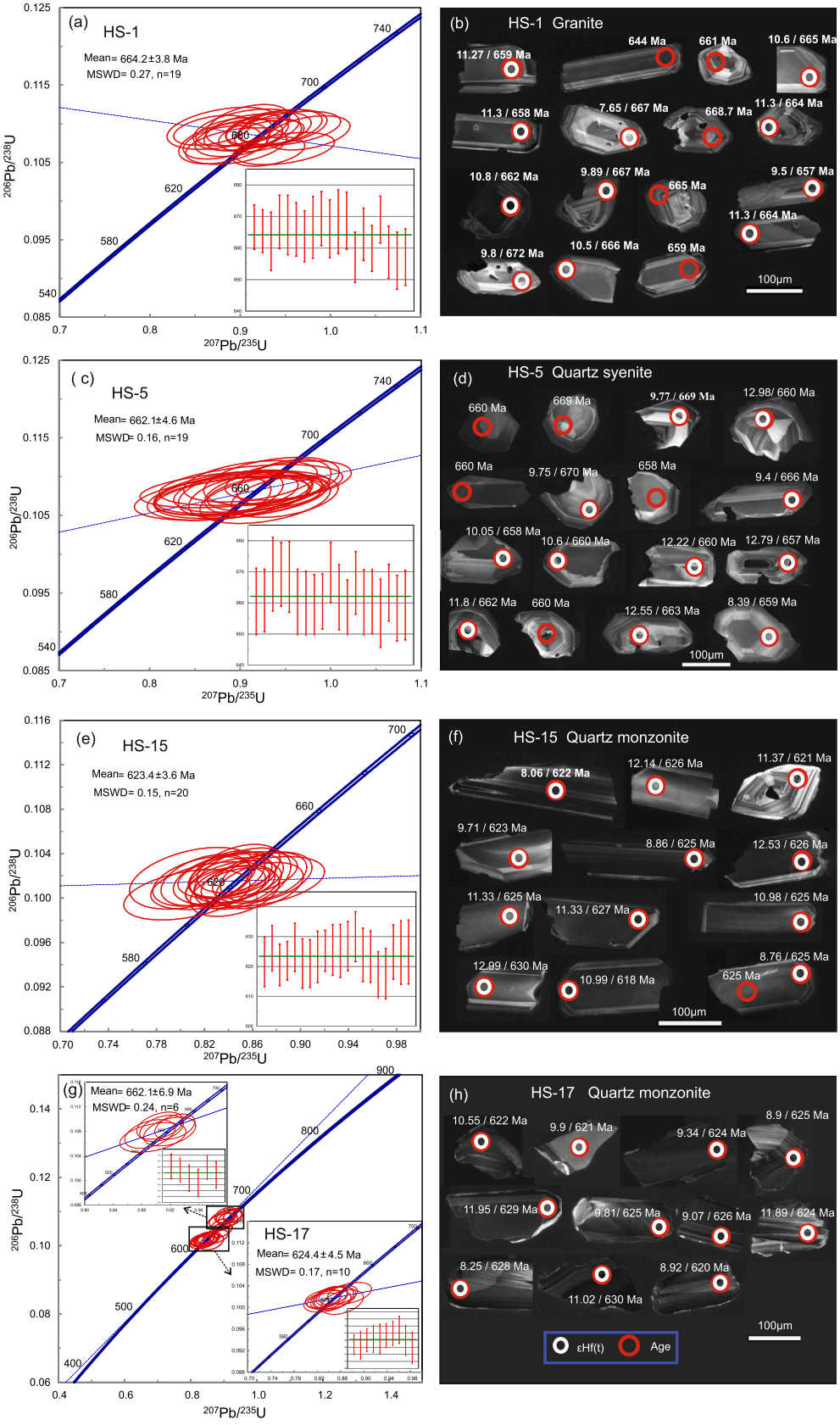

Fig. 5. LA-ICP-MS U-Pb zircon age Concordia diagrams (a, c, e, and g), and their representative cathodoluminescence (CL) images of dated zircons (b, d, f, and h) for the Neoproterozoic Hamisana Granitoids in the ANS.

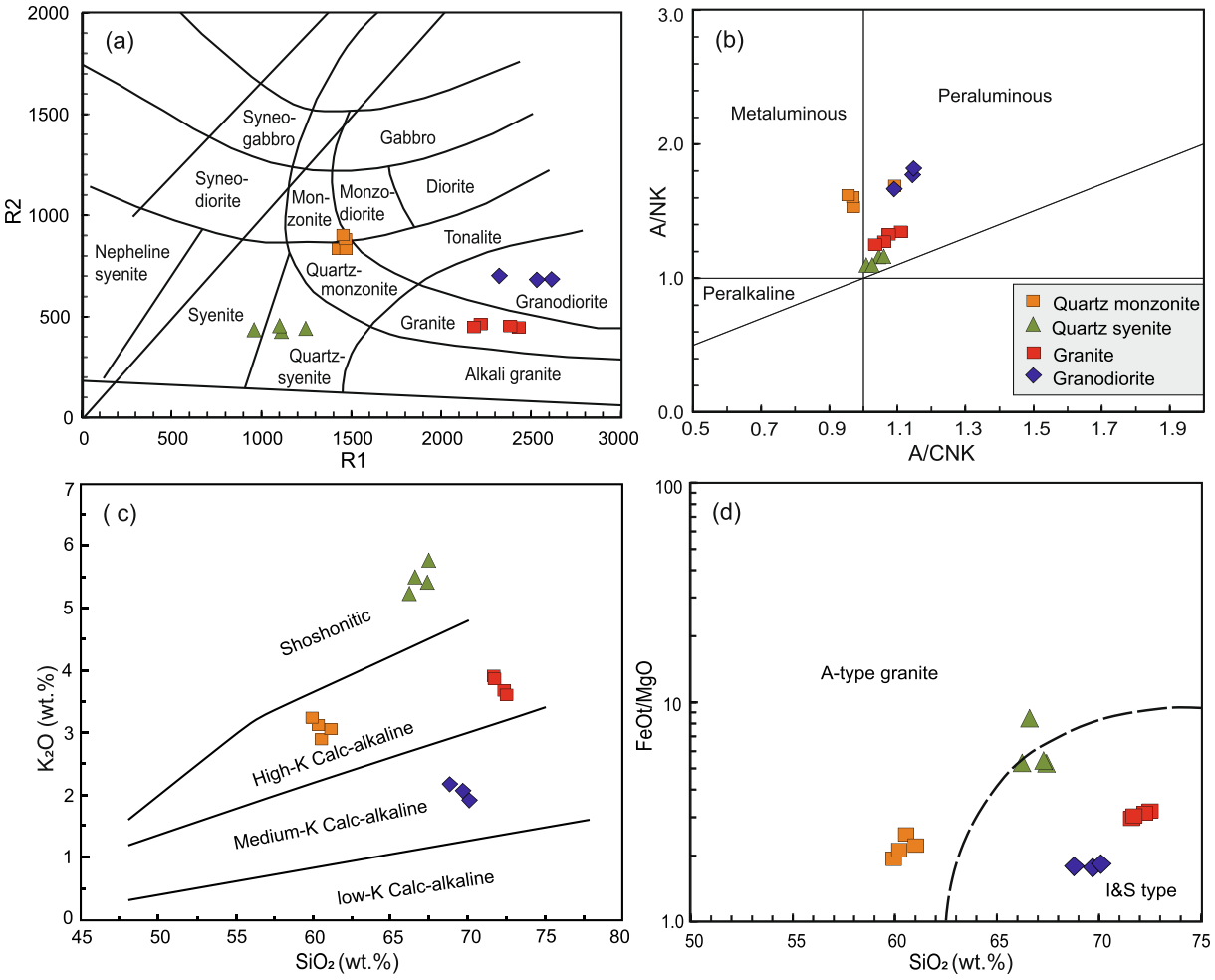

Fig. 6. (a) TAS diagram, plots of total alkalis vs. SiO_2 (Middlemost, 1994). (b) A/NK-A/CNK diagram (Maniar and Piccoli, 1989). (c) K_2O-SiO_2 diagram (solid line: Peccerillo and Taylor (1976). (d) SiO_2–FeOt/MgO diagram, for the Neoproterozoic Hamisana Granitoids plutons. Dotted line: Middlemost, (1985)); A/CNK. (Al_2O_3/(CaO + Na_2O + K_2O) molecular); A/NK. (Al_2O_3/(Na_2O + K_2O) molecular).

background and analyte signals, and time-drift correction and quantitative calibration for trace element analyses and U-Pb dating were performed by ICPMSDataCal (Liu et al., 2010a). Concordia diagrams and weighted mean calculations were made using Isoplot/Ex_ver3 (Ludwig, 2003).

4.2. Whole-rock major and trace element analyses

Whole-rock samples (n = 15) were crushed and powdered to b200-mesh in an agate mill. Major element abundances of these samples were obtained by X-ray fluorescence (XRF-1800) at the State Key Laboratory of Geological Processes and Mineral Resources (GPMR), China University of Geoscience (CUG), Wuhan. The accuracy and precision of the XRF data were assessed using Chinese national standards, and duplicate runs on selected samples of the XRF analyses are estimated to be ~1% for elements with concentrations N10 wt.% and 5% for the other major elements. More details about the XRF analytical procedure are given in Ma et al. (2012) and Wang et al. (2013).

Whole-rock trace element compositions were determined by inductively coupled plasma mass spectrometry (ICPMS) (Agilent 7500a ICP–MS), using the techniques described by Liu et al. (2008) and Qi et al. (2000). Pure Rb standard solution was used for internal calibration, and GSR-1, BHVO-2, and OU-6 were used as reference materials. The relative errors of the ICP-MS analyses are estimated to be better than ± 5–10% for most elements.

4.3. In situ Lu-Hf isotopes

Hf isotope behavior in granitoid rocks are strongly controlled by zircon (Belousova et al., 2010) because it is the principal host mineral of Hf (Ali et al., 2015) and Hf is an essential element in the crystal structure of zircon (Patchett and Tatsumoto, 1981). Present-day Hf isotopic compositions of zircons, which are characterized by low Lu/Hf ratios, approximate those of magmas from which they were crystallized (Kinny and Maas, 2003). Zircon also has strong resistance to re-equilibration of its Hf isotopic composition (Watson, 1996; Watson and Cherniak, 1997), and hence to any disturbance of its Hf isotopic system as a result of high–temperature magmatic processes or high-grade metamorphism (e.g., Huang et al. (2006), Lenting et al. (2010)). These features make zircon an ideal repository as a chronometer (U–Pb geochronology) and an isotopic tracer (Lu–Hf isotope system) (Kinny and Maas, 2003; Belousova et al., 2006, 2010; Lenting et al., 2010), particularly if/when the whole-rock isotopic systems were disturbed by earth processes (Belousova et al., 2010). Therefore, we conducted in-situ Lu-Hf isotope analyses of the dated zircon grains from our HSZ granitoid samples HS-1, HS-5, HS-15, and HS-17. We used a Neptune plus multi-collector (MC)-ICPMS system, in combination with a Geolas 2005 system in the GPMR–China University of Geosciences at Wuhan.

The zircons were ablated by a 193 nm ArF Laser system. The spot size of 50 μm was used for analysis, with a laser repetition rate of 10 Hz at 100 mJ/pulse. 179Hf / 177Hf = 0.7325 (Chu et al., 2002) was used to correct the instrument quality discrimination of Hf isotopes. The

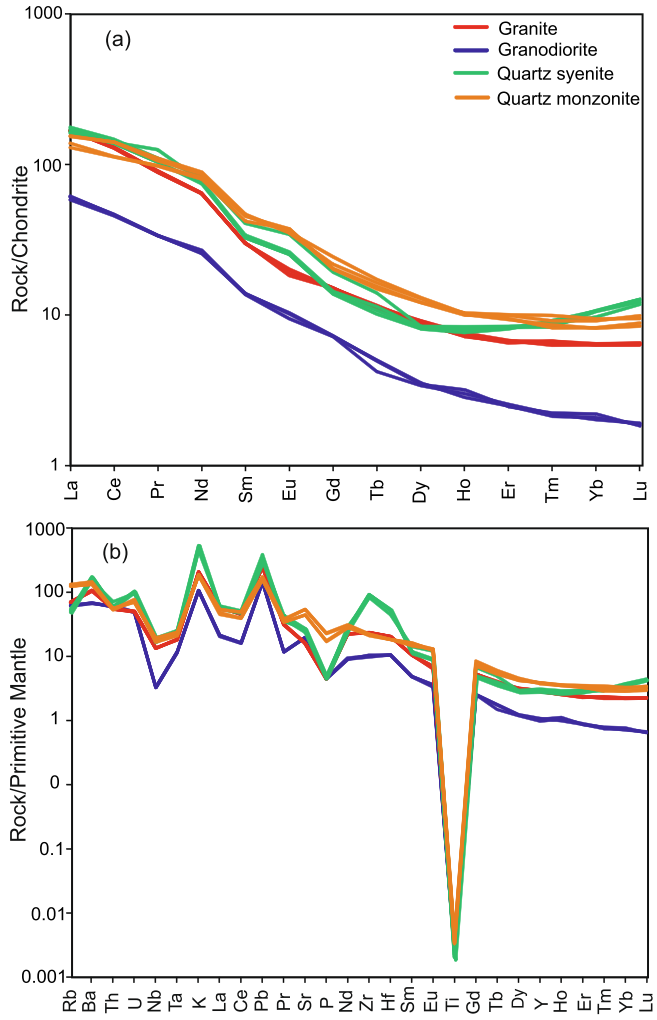

Fig. 7. (a) Chondrite-normalized REE patterns, and (b) primitive mantle-normalized trace element patterns for the Hamisana Granitoids in the ANS. Normalizing values are from Sun and McDonough (1989).

instrument quality discrimination factor for Yb isotopes was calculated using the relationship βYb = 0.8725 × βHf (Xu et al., 2004). The correction of 176Hf's heterogeneous interference by 176Lu and 176Yb was corrected using 176Yb / 172Yb = 0.5886 and 176Lu/175Lu = 0.02655 (Chu et al., 2002). The test result of the international standard zircon 91,500 is 0.282301 ± 0.000017 (2δ, n = 15), which is consistent with the published value of 0.282307 ± 0.000031 (Wu et al., 2006). The test result of Penglai zircon is 0.282915 ± 0.000014 (2δ, n = 18), which is consistent with the published value of 0.282906 ± 0.000010 (Li et al., 2010). The test result of Plešovice zircon is 0.282477 ± 11 (2δ, n = 18), which is consistent with the international recommended value of 0.282482 ± 0.000013 (Sláma et al., 2008). The test result of zircon in Qinghu granite is 0.283002 ± 0.000012 (2δ, n = 15), which is consistent with the reported value of 0.283002 ± 0.000004 (Li et al., 2013). Calculation methods for εHf(t), TDM1, and TDM2 values are similar to those of Wu et al. (2008). The detailed analytical procedure followed that described by Yuan et al. (2008).

4.4. Whole-rock Sr-Nd isotope analyses

Whole-rock Sr-Nd isotopic compositions were analyzed using a Finnigan Triton Ti thermal ionization mass spectrometer (TIMS) at GPMR. For details of the analytical procedures, see Wang et al. (2013). Powder samples (~100 mg) were dissolved in a Telfon bomb with a mixture of concentrated HNO3 acid and HF. The samples were dried in an oven at 190 °C for 48 h and then converted into chlorides by adding 1 ml of 6 N HCl and dissolved again in 1 ml of 2.5 N HCl. Nd was separated and purified from the final solution using the conventional cation-exchange technique. Mass fractionation for measured Nd isotopic ratios was normalized using a $^{146}Nd/^{144}Nd$ ratio of 0.7219. Analyses of standard BCR-2 yielded a mean $^{143}Nd/^{144}Nd$ ratio of 0.512655 ± 4. A^{47}Sm decay constant (λ) of 6.54 × 10–11 year − 1 was adopted for the calculations. We have used the depleted mantle models of Goldstein et al. (1984) in our calculations. Fix εNd(t) values were calculated relative to the chondritic uniform reservoir for a present-day $^{143}Nd/^{144}Nd$ ratio of 0.512638 and $^{147}Sm/^{144}Nd$ ratio of 0.1967. Single-stage (TDM1) Nd model age calculations utilized $^{143}Nd/^{144}Nd$ and $^{147}Sm/^{144}Nd$ ratios of 0.51315 and 0.2137, respectively, for the present-day depleted mantle.

5. U-Pb zircon ages of the HSZ granitoids

Four HSZ granitoid samples, including granite (HS-1), quartz syenite (HS-5), and quartz monzonite rocks (HS-15 and HS-17), were used for zircon dating. The results are listed in Table 2. Concordia diagrams and the representative CL images are presented in Fig. 5. Age calculations were done, following Goldstein et al. (1984).

Twenty U-Pb spot analyses were acquired on 19 zircon grains selected from sample HS-1 (granite). They have U contents of 60.6 to 447 ppm and Th contents of 39.3 to 503 ppm (Table 2). They have yielded a concordant U-Pb age with a weighted mean $^{206}Pb/^{238}U$ age of 664.2 ± 3.8 Ma (MSWD = 0.27, 95% confidence interval) (Fig. 5a). Zircon grains from this granite sample are mainly dark gray to slightly colorless, euhedral to subhedral, transparent with short to long prismatic forms. Their crystal lengths mostly vary from 100 to 220 μm, with aspect ratios of 1:1 to 2:1 (Fig. 5b). CL images show that the majority of zircon grains have continuous oscillatory zoning textures, consistent with growth from surrounding magma with inherited cores in the center. These textures indicate a magmatic origin, as described by Wu and Zheng (2004).

Twenty U-Pb spot analyses were done on 19 zircon grains, selected from sample HS-5 (quartz syenite). They have U contents of 31.1 to 125 ppm and Th contents of 24.5 to 142 ppm (Table 2). They have yielded concordant U-Pb ages with a weighted mean $^{206}Pb/^{238}U$ age of 662.1 ± 4.6 Ma (MSWD = 0.16, 95% confidence interval) (Fig. 5c). Zircon grains from this sample (HS-5) are mainly dark gray to slightly colorless, euhedral to subhedral, transparent with short rounded to long prismatic forms. Their crystal lengths mostly vary from 100 to 200 μm, with aspect ratios of 1:1 to 1.5:1 (Fig. 5d). CL images show that the majority of zircon grains have continuous oscillatory zoning textures, consistent with their growth from surrounding magmas. These textures indicate a magmatic origin.

Twenty data points were obtained on 19 zircon grains from sample HS-15 (quartz monzonite). They display U contents of 76.6 to 289 ppm and Th contents 35.7 to 311 ppm, supporting their magmatic origin. They have yielded concordant U-Pb ages with a weighted mean $^{206}Pb/^{238}U$ age of 623.4 ± 3.6 Ma (MSWD = 0.15, 95% confidence interval (Fig. 5e). Zircon grains from this sample (HS-15) are dark, gray to colorless, and most of the grains are euhedral with long prismatic and subhedral shapes, transparent to translucent. Their crystal lengths commonly vary from 120 to 300 μm, with aspect ratios of 1:1 to 3:1 (Fig. 5f). The CL images show that most of the zircon grains have clear parallel and oscillatory zoning.

Twenty data points were obtained on 19 zircon grains from sample HS-17 (quartz monzonite). They display U contents of 140 to 1955 ppm and Th contents 47.5 to 655 ppm. The analyzed zircons have provided concordant U-Pb ages that fall into two groups: the first group represents the majority of the analyzed grains with a weighted mean $^{206}Pb/^{238}U$ age of 624.4 ± 4.5 Ma (MSWD = 0.17, 95% confidence interval), and the second group has a weighted mean $^{206}Pb/^{238}U$ age of

Table 3
Lu-Hf isotopic data of the Hamisana granitoids in the Arabian-Nubian Shield.

Spot	176Hf/177Hf	2σ	176Yb/177Hf	2σ	176Lu/177Hf	2σ	age	Hf(I)	2σ	εHf(0)	2σ	εHf(t)	2σ	T(DM)1	2σ	T(DM)2	2σ
HS-1 Granite																	
1	0.2827006	0.0000258	0.0271079	0.000252	0.001066997	0.00000892	659	0.2827006	1.52	−2.98	0.91	11.27	0.91	782.48	36.47	1248.40	58.18
2	0.2826971	0.000033	0.01610743	0.000115	0.000682716	0.00000484	658	0.2826971	1.59	−3.11	1.17	11.30	1.17	779.47	46.17	1256.38	74.41
3	0.2825845	0.0000284	0.01039915	0.0000988	0.000456113	0.00000457	669	0.2825845	1.58	−7.09	1.00	7.65	1.00	931.28	39.38	1510.10	63.86
4	0.2826757	0.0000269	0.02051831	0.0000347	0.000870257	0.00000143	665	0.2826757	1.72	−3.87	0.95	10.61	0.95	813.42	37.80	1304.60	60.62
5	0.2827328	0.0000298	0.0315458	0.000195	0.001281533	0.00000773	662	0.2827328	1.81	−1.85	1.05	11.32	1.05	741.17	42.39	1175.68	67.25
6	0.2826965	0.0000267	0.05289837	0.000359	0.001929033	0.0000163	662	0.2826965	2.12	−3.13	0.94	10.81	0.94	806.77	38.61	1257.43	60.18
7	0.2826475	0.0000333	0.01199586	0.0000423	0.000488637	0.00000138	670	0.2826475	1.62	−4.86	1.18	9.89	1.18	844.53	46.29	1368.26	75.00
8	0.2826512	0.0000752	0.02587348	0.000128	0.001036623	0.00000473	672	0.2826512	7.38	−4.73	2.66	9.82	2.66	851.60	106.00	1359.77	169.25
9	0.2826686	0.0000324	0.01240668	0.000311	0.00054319	0.0000124	666	0.2826686	1.67	−4.12	1.15	10.53	1.15	816.34	45.13	1320.69	73.01
10	0.2826462	0.0000417	0.02632967	0.000154	0.001108937	0.00000501	668	0.2826462	1.12	−4.91	1.47	9.53	1.47	860.30	58.91	1371.01	93.88
11	0.2826918	0.0000304	0.02062377	0.000317	0.000846386	0.0000129	670	0.2826918	1.67	−3.30	1.08	11.30	1.08	790.29	42.71	1268.30	68.54
12	0.2826085	0.0000432	0.0186827	0.0000394	0.000738683	0.00000152	664	0.2826085	1.34	−6.24	1.53	8.27	1.53	904.66	60.38	1456.01	97.17
HS-5 Quartz syenite																	
1	0.2826519	0.0000437	0.02607785	0.0000328	0.001054795	0.000000916	669	0.2826519	1.42	−4.71	1.55	9.77	1.55	851.02	61.65	1358.18	98.39
2	0.2827654	0.0000358	0.03351686	0.0000832	0.001398195	0.00000246	660	0.2827654	1.57	−0.69	1.27	12.98	1.27	696.93	51.13	1102.03	80.85
3	0.2826499	0.0000366	0.02368436	0.000111	0.000994991	0.00000508	670	0.2826499	1.45	−4.78	1.29	9.75	1.29	852.49	51.56	1362.71	82.41
4	0.2827182	0.0000309	0.03588331	0.000104	0.00142821	0.00000256	662	0.2827182	1.49	−2.36	1.09	11.80	1.09	764.94	44.11	1208.60	69.70
5	0.2826743	0.0000343	0.04217851	0.000291	0.001692919	0.00001	658	0.2826743	2.09	−3.91	1.21	10.05	1.21	833.52	49.25	1307.53	77.26
6	0.2826432	0.000031	0.02521249	0.000616	0.001063463	0.0000224	666	0.2826432	1.75	−5.01	1.10	9.40	1.10	863.50	43.74	1377.78	69.79
7	0.2826849	0.0000283	0.03351786	0.0000423	0.001357958	0.000000874	660	0.2826849	1.69	−3.54	1.00	10.61	1.00	810.95	40.29	1283.73	63.78
8	0.2827301	0.0000415	0.03420736	0.000293	0.001337243	0.00000861	660	0.2827301	1.20	−1.94	1.47	12.22	1.47	746.12	59.11	1181.77	93.63
9	0.2827970	0.00003	0.03072435	0.00029	0.001253956	0.0000111	657	0.282797	1.64	0.42	1.06	12.79	1.06	649.24	42.72	1030.63	67.81
10	0.2827361	0.0000396	0.02938406	0.0000784	0.001231367	0.00000234	663	0.2827361	1.52	−1.73	1.40	12.55	1.40	735.48	56.26	1168.24	89.36
11	0.2826133	0.0000361	0.01438268	0.0000288	0.000603742	0.000000576	659	0.2826133	1.53	−6.07	1.28	8.39	1.28	894.77	50.29	1445.25	81.22
HS-15 Quartz monzonite																	
1	0.2826289	0.000034	0.01909378	0.000123	0.000759203	0.00000468	622	0.2826289	1.65	−5.52	1.20	8.1	1.20	876.60	47.57	1410.08	76.53
2	0.2827456	0.0000317	0.02790975	0.000468	0.001091449	0.0000107	626	0.2827456	1.45	−1.39	1.12	12.1	1.12	719.29	44.88	1146.82	71.56
3	0.2827228	0.000035	0.0171994	0.000103	0.000727379	0.00000432	621	0.2827228	1.45	−2.20	1.24	11.4	1.24	744.36	49.05	1198.38	78.97
4	0.2826795	0.0000278	0.02880057	0.000334	0.001134852	0.000013	623	0.2826795	1.80	−3.73	0.98	9.7	0.98	813.78	39.34	1295.96	62.65
5	0.2826541	0.0000381	0.0289839	0.00014	0.001129943	0.0000567	625	0.2826541	1.36	−4.63	1.35	8.9	1.35	849.61	53.87	1353.21	85.79
6	0.2827606	0.0000341	0.03653141	0.00026	0.001424006	0.00000938	626	0.2827606	1.39	−0.86	1.21	12.5	1.21	704.27	48.73	1112.87	77.00
7	0.2827284	0.0000242	0.0391207	0.00033	0.001522014	0.0000125	625	0.2827284	1.73	−2.00	0.86	11.3	0.86	752.27	34.65	1185.56	54.60
8	0.2827265	0.0000551	0.03732296	0.000114	0.001468524	0.00000392	627	0.2827265	1.14	−2.07	1.95	11.3	1.95	753.90	78.74	1189.86	124.27
9	0.282769	0.0000337	0.03166444	0.000443	0.00123429	0.0000164	630	0.282769	1.59	−0.57	1.19	13.0	1.19	688.75	47.93	1093.93	76.12
10	0.2827202	0.0000262	0.03292107	0.000228	0.001285754	0.00000867	618	0.2827202	1.88	−2.29	0.93	11.0	0.93	759.18	37.27	1204.12	59.11
11	0.2826478	0.0000389	0.02101834	0.0000619	0.000834601	0.00000276	625	0.2826478	1.71	−4.85	1.38	8.8	1.38	851.83	54.56	1367.49	87.59
12	0.2826651	0.0000401	0.01494066	0.00005	0.000615255	0.00000167	625	0.2826651	1.32	−4.24	1.42	9.5	1.42	822.77	55.95	1328.56	90.34
HS-17 Quartz monzonite																	
1	0.2826984	0.0000266	0.0163723	0.000015	0.000666124	0.000000556	622	0.2826984	2.10	−3.06	0.94	10.55	0.94	777.31	37.20	1253.46	59.99
2	0.2826768	0.0000306	0.008402324	0.000098	0.000349621	0.00000411	621	0.2826768	1.89	−3.83	1.08	9.90	1.08	800.85	42.42	1302.25	68.98
3	0.2826589	0.0000201	0.00769988	0.000437	0.000326843	0.00000195	624	0.2826589	3.11	−4.46	0.71	9.34	0.71	825.18	27.84	1342.61	45.29
4	0.2826438	0.0000407	0.01525244	0.0000384	0.000630661	0.000000916	625	0.2826438	1.54	−4.99	1.44	8.70	1.44	852.84	56.78	1376.56	91.64
5	0.2827337	0.0000316	0.01799966	0.0000918	0.000700752	0.0000033	629	0.2827337	1.97	−1.81	1.12	11.95	1.12	728.56	44.27	1173.78	71.32

(*continued on next page*)

Table 3 (*continued*)

Spot	176Hf/177Hf	2σ	176Yb/177Hf	2σ	176Lu/177Hf	2σ	age	Hf(I)	2σ	εHf(0)	2σ	εHf(t)	2σ	T(DM)1	2σ	T(DM)2	2σ
6	0.2826812	0.0000467	0.0299521	0.0000968	0.001137054	0.00000343	625	0.2826812	1.46	−3.67	1.65	9.81	1.65	811.42	66.08	1292.13	105.22
7	0.2826514	0.0000328	0.01184075	0.0000318	0.000484776	0.00000113	626	0.2826514	1.84	−4.72	1.16	9.07	1.16	839.02	45.60	1359.47	73.88
8	0.2826296	0.0000349	0.01607883	0.000047	0.000660659	0.00000158	628	0.2826296	1.83	−5.50	1.23	8.25	1.23	873.35	48.71	1408.53	78.56
9	0.2827082	0.0000337	0.02090423	0.0000785	0.000806537	0.0000028	630	0.2827082	1.83	−2.72	1.19	11.02	1.19	766.43	47.31	1231.31	76.01
10	0.2827381	0.0000311	0.02448385	0.000467	0.000929976	0.0000171	624	0.2827381	1.66	−1.66	1.10	11.89	1.10	726.79	43.84	1163.79	70.20
11	0.2826487	0.0000241	0.005732078	0.0000228	0.000238812	0.000000764	620	0.2826487	2.08	−4.82	0.85	8.92	0.85	837.39	33.29	1365.63	54.29

In-situ Lu-Hf isotope analyses conducted on the dated zircon grains by using a Neptune plus multi-collector (MC)-ICPMS system, in combination with a Geolas 2005 system in the GPMR–China University of Geosciences at Wuhan. Initial Hf isotope ratios were calculated with reference to the chondritic ratio at the time of crystallization assumed for each sample, a decay constant for 176Lu of 1.867×10^{-11} (Scherer et al., 2001, 2007), and the chondritic ratios of 176Hf/177Hf (0.282772) and 176Lu/177Hf (0.0332) (Blichert-Toft and Albaréde, 1997) were used. Single-stage Hf model ages (tDM) were calculated using the measured ratios, referred to a model depleted Mantle with present-day 176Hf/177Hf of 0.28325 and 176Lu/177Hf of 0.0384 (Vervoort and Blichert-Toft, 1999). Two-stage Hf model ages (tDMc) are calculated assuming a mean 176Lu/177Hf value of 0.015 of average continental crust (Griffin et al., 2002). Hf model ages (tNC) are calculated from the new crust assuming of 0.0113 (Dhuime et al., 2011) for average continental crust and a juvenile crust 176Lu/177HfNC and 176Hf/177HfNC of 0.0384 and 0.283165, respectively (Chauvel et al., 2008).

Table 4
Whole rock Sr-Nd isotopic results of the Hamisana granitoids in the Arabian-Nubian Shield.

Sample No.	Age (Ma)	Rb (ppm)	Sr (ppm)	$^{87}Rb/^{86}Sr$	$^{87}Sr/^{86}Sr$	2σ	$(^{87}Sr/^{86}Sr)_i$	Sm (ppm)	Nd (ppm)	$^{147}Sm/^{144}Nd$	$^{143}Nd/^{144}Nd$	2σ	$(^{143}Nd/^{144}Nd)_i$	εNd(t)	T_{DM} (Ga)
HS-1	664.2	44.3	332	0.386130115	0.706222	4	0.702632828	4.55	30.1	0.091265874	0.512447	3	0.512049691	5.24	0.877
HS-5	662.1	36.5	115	0.918961197	0.711735	5	0.703220166	10.2	97.0	0.063486606	0.512351	2	0.512075498	5.69	0.813
HS-10	642.0	31.1	572	0.157309268	0.704384	12	0.702970864	4.95	35.5	0.08418669	0.512477	9	0.512122784	6.10	0.794
HS-15	623.4	48.7	327	0.430979645	0.706399	6	0.702640092	6.12	41.2	0.08968569	0.512500	19	0.512133602	5.85	0.801
HS-17	624.4	47.9	331	0.418775684	0.706361	8	0.702708532	7.12	41.6	0.103338138	0.512549	2	0.512126827	5.71	0.862
P2-5	623.4	55.3	827	0.193466299	0.704284	10	0.702596630	4.92	26.4	0.112522175	0.512578	2	0.512118307	5.55	0.864

Whole-rock Sr-Nd isotopic compositions were analyzed using a Finnigan Triton Ti thermal ionization mass spectrometer (TIMS) at GPMR. Analyses of standard BCR-2 yielded a mean 143Nd/144Nd ratio of 0.512655 ± 4. A^{47}Sm decay constant (λ) of 6.54 × 10–11 year − 1 was adopted for the calculations. εNd(t) and Sr(i) were calculated for an age of rock formation. The εNd(t) values were calculated relative to the chondritic uniform reservoir for a present-day143Nd/144Nd ratio of 0.512638 and 147Sm/144Nd ratio of 0.1967. Single-stage (TDM1) Nd model age calculations utilized 143Nd/144Nd and 147Sm/144Nd ratios of 0.51315 and 0.2137, respectively, for the present-day depleted mantle.

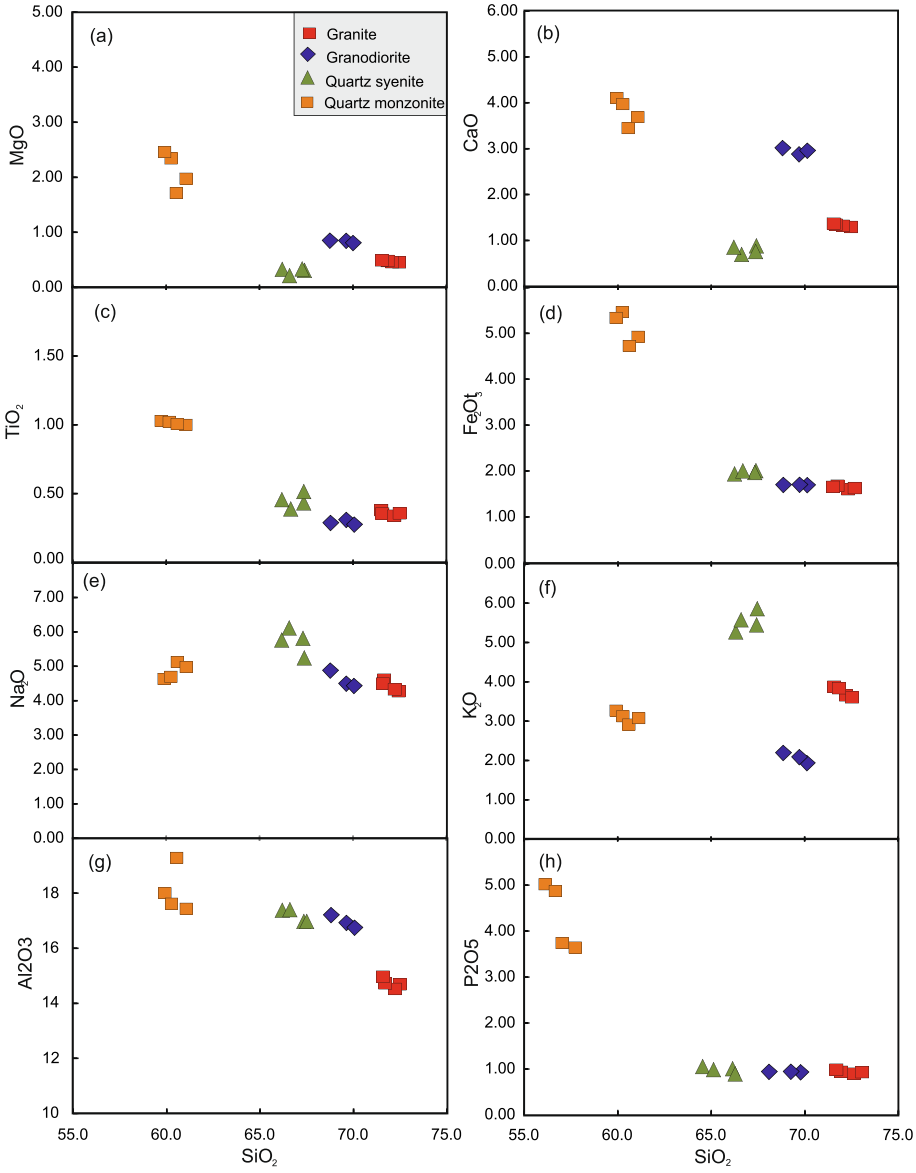

Fig. 8. Selected major element oxide concentrations vs. SiO_2 (wt%) of the Harker diagram in the granitoids of the Hamisana Shear Zone.

662.1 ± 6.9 Ma; MSWD = 0.24 (Fig. 5g). Zircon grains from the quartz monzonite sample (HS-17) are mostly dark gray to almost colorless and have euhedral to subhedral habits with long prismatic forms. Their crystal lengths commonly vary from 40 to 150 μm, with crystal length/width ratios of 1:1 to 1.5:1. The majority of zircon grains exhibit sector or fully-developed oscillatory zoning features, whereas the others show parallel and oscillatory zoning textures (Fig. 5h).

6. Whole-rock major and trace element chemistry of the HSZ granitoids

Whole-rock major- and trace-element, and REE compositions of representative HSZ granitoid samples are listed in Table 1.

6.1. Major-element geochemistry

The compositional ranges of selected major oxide components of granite and granodiorite samples are: SiO_2 (72.5–71.6 wt%) and (70.1–68.8 wt%); Al_2O_3 (14.9–14.5 wt%) and (17.2–16.8 wt%); magnesium number (Mg# = 37.4–35.9 and 50.4–49.3), and Na_2O (4.57–4.25 wt%) and (4.83–4.39 wt%), respectively.

The selected compositional ranges of the quartz syenite and quartz monzonite samples are as follows: SiO_2 (67.4–66.2 wt%) and (61.1–60.0 wt%); K_2O (5.8–5.2 wt%) and (3.2–2.9 wt%) respectively. The quartz syenite samples show relatively low magnesium numbers (Mg# = 25.3–17.4), whereas the quartz monzonite samples display high MgO contents (2.46–1.72 wt%) with high magnesium numbers (Mg# = 47.8–42.0) (Table 1).

All analyzed HSZ granitoid samples, HS-1, HS-5, HS-15, and HS-17, plot in the granite, granodiorite, quartz syenite, and quartz monzonite fields, respectively, as shown in the T1-T2 diagram (Fig. 6a) (de la Roche et al., 1980). However, these samples have A/CNK (Al_2O_3/CaO + Na_2O + K_2O molecular basis) ratios between 1.14 and 0.96, and A/NK values ranging from 1.78 to 1.07 (Table 1), except the quartz monzonite samples with an average A/CNK value of 1.0 and an average A/NK value of 1.60. Therefore, in the A/NK–A/CNK diagram the majority of the granitoid samples represent peraluminous, calc-alkaline granites, whereas the quartz monzonite samples characterize predominantly metaluminous compositions (Maniar and Piccoli, 1989; Fig. 6b). Granodiorite samples belong to the medium-K sub-alkaline series, whereas granite, quartz monzonite, and quartz syenite plot in high-K calc-alkaline to shoshonitic fields in the SiO_2–K_2O diagram

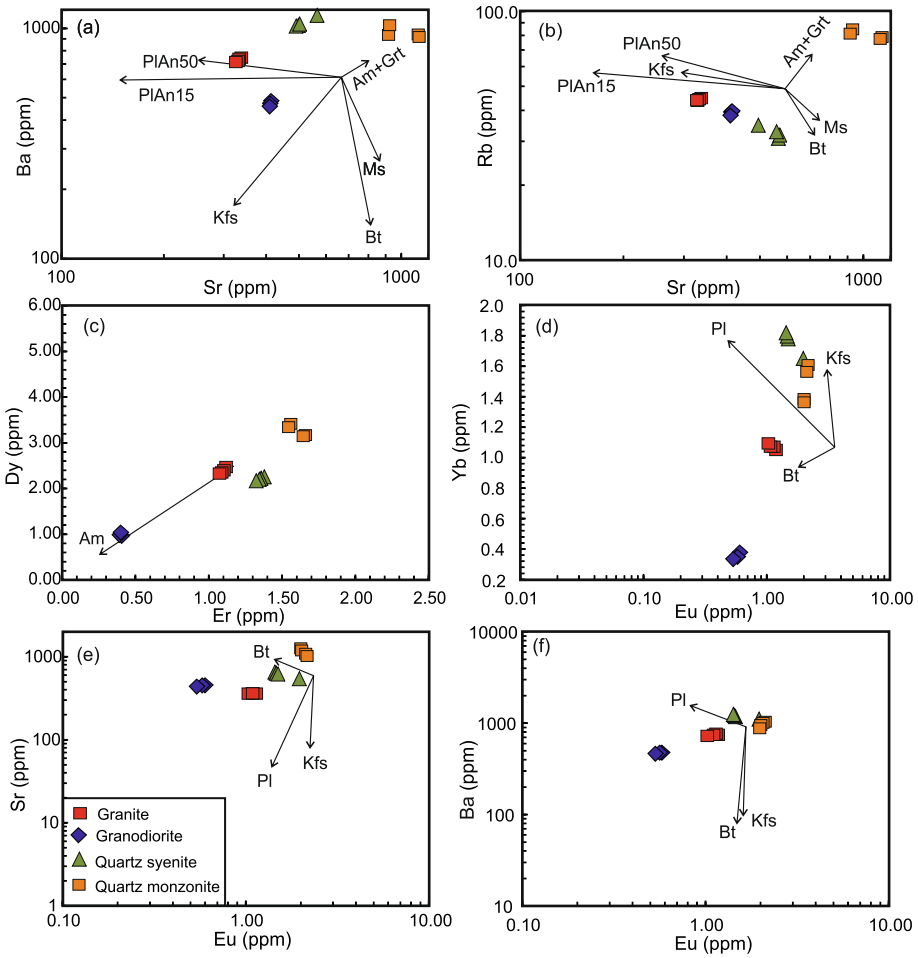

Fig. 9. (a) Sr versus Ba, (b) Rb, (c) Er versus Dy, (d) Eu versus Yb, (e) Sr, and (f) Ba diagrams for Neoproterozoic HSZ granitoids. Am = Amphibole; Grt = Garnet; Kfs = K-feldspar; Pl = Plagioclase; PlAn50 and PlAn15 = Plagioclase (anorthosite 50 and 15); Bt = Biotite; Ms = Muscovite.

(Fig. 6c).

6.2. Trace and REEs geochemistry

Results of the trace element analyses are shown in Table 1. All four groups of rock types are strongly enriched in incompatible elements. The total REE abundances of granodiorite, granite, quartz syenite, and quartz monzonite samples are in the range of 69.5–67.6 ppm, 186.3–183.9 ppm, 214.1–197.2 ppm, and 214.5–171.2 ppm, respectively. They show a flat pattern with no significant Eu anomalies in chondrite-normalized REE patterns, except for the quartz syenite samples, which display enrichments in Y and Lu (Fig. 7a) (Sun and McDonough, 1989). The spider diagram of trace elements normalized to primitive mantle shows that all samples have similar REE patterns and exhibit selective enrichment in the large ion lithophile elements (LILE) of Rb, Ba, K, Pb, and Sr, and are depleted in the high-field strength elements (HFSE) of Nb, Ta, Sm, P, and Ti, (Fig. 7b). The (La/Yb)N and (Gd/Yb)N ratios for these samples are given in Table 1.

7. Zircon Lu-Hf isotope compositions

Zircon grains from four HSZ granitoid samples (HS-1, HS-5, HS-15, and HS-17) that were used for U-Pb dating were also selected for Lu-Hf isotope analysis. The results are listed in Table 3. Initial $^{176}Hf/^{177}Hf$ ratios and $\varepsilon_{Hf}(t)$ values were calculated from the formation age (Ma) of these samples. Twelve (12) selected zircon grains from sample HS-1 yielded $^{176}Hf/^{177}Hf$ ratios, varying from 0.2826 to 0.2827. Their corresponding $\varepsilon_{Hf}(t)$ values range from +11.32 to +7.65, yielding a weighted mean value of +10.36. Single-stage Hf model ages vary from 0.74 to 0.93 Ga and two-stage Hf model ages from 1.1 to 1.5 Ga, with a mean TDM2 age of 1.3 Ga (Table 3).

Eleven (11) selected zircon grains from sample HS-5 yielded $^{176}Hf/^{177}Hf$ ratios varying from 0.2826 to 0.2828. Their corresponding $\varepsilon_{Hf}(t)$ values range from +12.98 to + 8.39, yielding a weighted mean value of +10.10. Single-stage Hf model ages vary from 0.65 to 0.89 Ga, and two-stage Hf model ages range from 1.0 to 1.4 Ga, with a mean TDM2 age of 1.2 Ga (Table 3).

Selected twelve (12) zircon grains from sample HS-15 have $^{176}Hf/^{177}Hf$ ratios varying from 0.2826289 to 0.2827606 with $\varepsilon_{Hf}(t)$ values of +13.0 to + 8.1, yielding a weighted mean value of +10.73. The single-stage Hf model ages vary from 0.68 to 0.88 Ga, and the two-stage Hf model ages from 1.09 to 1.40 Ga, with a mean TDM2 age of 1.25 Ga (Table 3).

Eleven (11) zircon grains from sample HS-17 display $^{176}Hf/^{177}Hf$ ratios varying from 0.2826 to 0.2827. Their corresponding $\varepsilon_{Hf}(t)$ values range from +11.95 to + 8.25, yielding a weighted mean value of +9.9. Single-stage Hf model ages vary from 0.73 to 0.87 Ga, and the two-stage Hf model ages from 1.16 to 1.40 Ga, with a mean TDM2 age of 1.28 Ga (Table 3).

8. Whole-rock Sr-Nd isotope compositions

Whole-rock Sr-Nd isotopic compositions of six (6) HSZ granitoid samples are provided in Table 4. The granite sample (HS-1) displays a $^{143}Nd/^{144}Nd$ ratio of 0.512447, corresponding to εNd(t) values of +5.24 at t = 664.2 Ma. This sample has yielded a single-stage

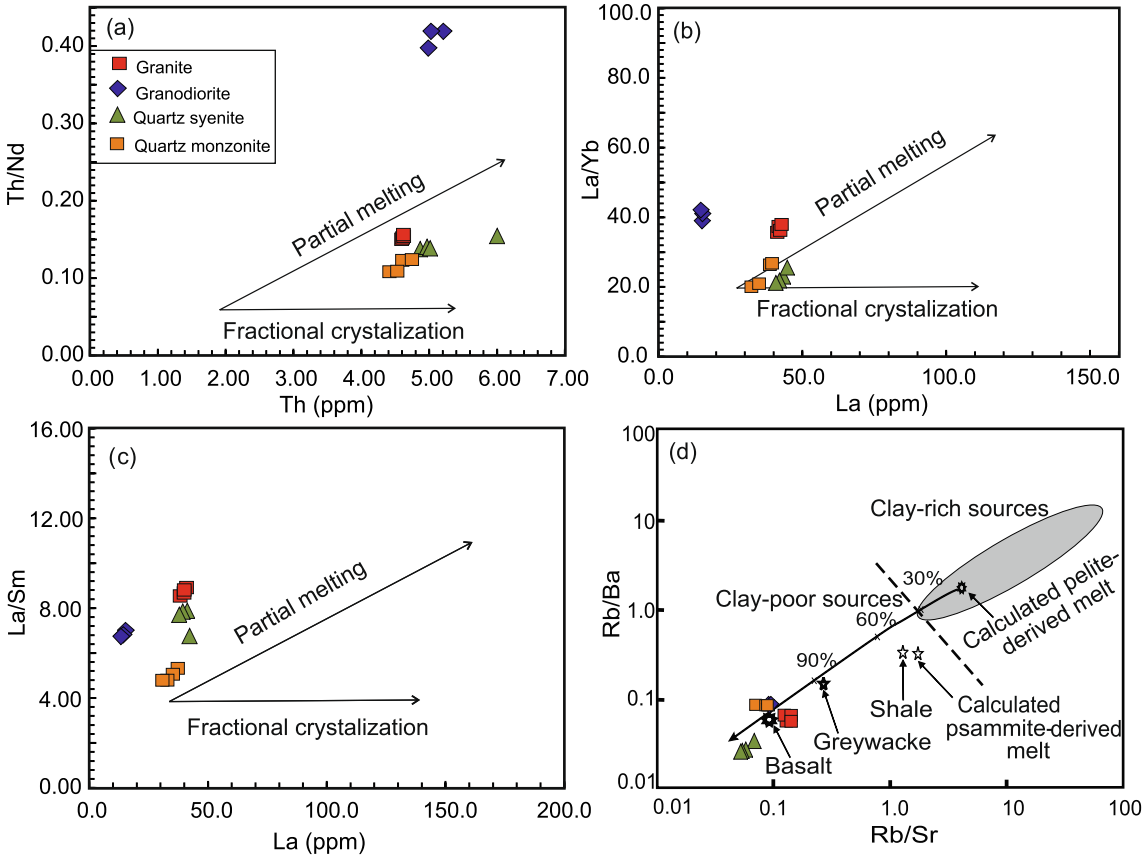

Fig. 10. (a) Th vs. Th/Nd, (b) La vs. La/Yb, (c) La/Sm, (d) Rb/Sr vs. Rb/Ba diagrams that demonstrate fractional crystallization and partial melting effects on the melt evolution of the Neoproterozoic HSZ granitoids.

depleted-mantle model age (TDM1) of 877 Ma. The two quartz syenite samples (HS-5 and HS-10) display $^{143}Nd/^{144}Nd$ ratios of 0.512351 and 0.512477, corresponding to εNd(t) values of +5.69 and +6.10 at t = 662.2 and 642 Ma, respectively. Single-stage depleted-mantle model ages (TDM1) of these samples are 812 and 794 Ma, respectively (Table. 4). The three quartz monzonite samples (HS-15, HS-17 and P2-5) display relatively high $^{143}Nd/^{144}Nd$ ratios of 0.5122500, 0.512549 and 0.512578, corresponding to εNd(t) values of +5.85–+5.71 and +5.55, at t = 623.4 and 624.4 Ma. Single-stage depleted-mantle model ages (TDM1) of these quartz monzonite samples are in the range of 800–864 Ma (Table 4).

9. Discussion

9.1. Timing of the emplacement of the HSZ granitoids

The ANS represents one of the largest tracts of juvenile Neoproterozoic crust in the earth. Amalgamation of different arc terranes within the ANS occurred between ~780 Ma and 600 Ma (El-Rahman et al., 2009a,b; Johnson (2014)). There appears to be a strong correspondence between the timing of deformation and igneous activity within the HSZ (550–660 Ma) based on limited geochronological data (Stern et al., 1989). However, the magmatic ages of many arc assemblages in the ANS are still not well established, and timing of most of the collisional and metamorphic events that took place during its assembly is still not well constrained.

9.1.1. Pre-existing age data and interpretations

Limited age data from the HSZ plutonic rock exist. A large body of gneissic granodiorite (sample GG-47) in the northern HSZ has been dated at 659 ± 62 Ma based on Rb-Sr whole – rock analysis (Stern et al., 1989; Stern and Kröner, 1993). A gneissic rock sample from the same area also yielded a U-Pb zircon discordia upper intercept age of 663 ± 29 Ma (Stern et al. 1989). Emplacement of the Shab granodiorite and the Ibib gneissic granite within the HSZ occurred ~645–660 Ma (Stern et al. 1989). The zircon and Rb-Sr whole-rock ages of ~660 Ma granitic rocks from NE Sudan and SE Egypt are interpreted as the mean ages of the emplacement of their magmas, and as the upper age limits for the initiation of magmatism within the HSZ (Stern et al. 1989).

Post-tectonic granitoids with varying compositions that occur within and across the HSZ revealed younger ages of emplacement. A large pluton with a monzodioritic rim and a K-feldspar porphyry granite core provided upper intercept ages of 611 ± 6, 608 ± 27 Ma, and 607 ± 16 Ma (Stern et al., 1989). The Allaqi granodiorite within the central part of the HSZ shows a strong ~N – S – oriented fabric (foliation), parallel to the general structure of the HSZ, and its emplacement has been interpreted to have taken place prior to HSZ deformation; this pluton gave a Rb-Sr errorchron age of 615 ± 121 Ma (MSWD = 9.7; Stern et al., 1989).

9.1.2. New age data and interpretations

Our new in-situ LA-ICP-MS U-Pb zircon dating of the four granitoid samples (HS-1, HS-5, HS-15, and HS-17) from the northern part of the HSZ provide significant time constraints for the timing of magmatism and deformation within the HSZ and for the evolution history of the ANS.

Zircon CL images for the selected granitoid samples show idiomorphic habits and oscillatory zoning textures, characteristic of *in-situ*, magmatic origin (Fig. 5). Selected twenty (20) U-Pb spot analyses of the granite sample (HS-1) (Table 2) have yielded concordant U-Pb ages with a weighted mean $^{206}Pb/^{238}U$ age of 664.2 ± 3.8 Ma

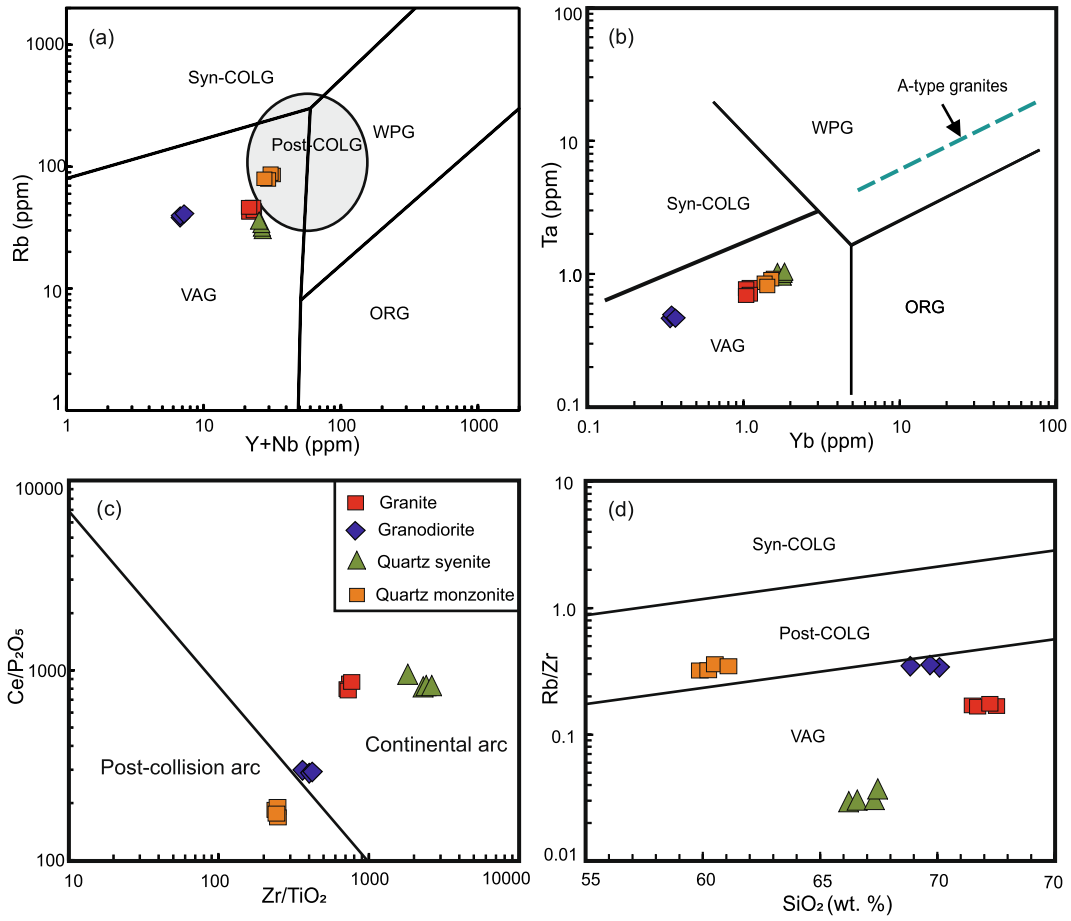

Fig. 11. Geochemical tectonic discrimination diagrams for Neoproterozoic HSZ granitoids. (a) Y + Nb vs. Rb. (b) Yb-Ta tectonic discrimination diagrams (after Pearce et al. (1984)). (c) Zr/TiO_2 vs. Ce/P_2O_3 and SiO_2 vs. Rb/Zr Diagrams. VAG = Volcanic arc granite; WPG = Within plate granite; S-COLG = Syn-collision granite; ORG = Ocean ridge granite.

(MSWD = 0.27, 95% confidence interval) (Fig. 5a). This age represents the timing of the emplacement of granitic intrusions in the study area.

U-Pb zircon dating analyses of the quartz syenite sample (HS-5) (Table 2) has yielded concordant U-Pb ages with a weighted mean $^{206}Pb/^{238}U$ age of 662.1 ± 4.6 Ma (MSWD = 0.16, 95% confidence interval) (Fig. 5c). We interpret this age as the timing of the emplacement of the quartz syenite intrusions.

Twenty data points were obtained for the quartz monzonite sample (HS-15) (Table 2). The analyses have yielded a concordant, weighted mean $^{206}Pb/^{238}U$ age of 623.4 ± 3.6 Ma (MSWD = 0.15, 95% confidence interval (Fig. 5e). We interpret this age as the timing of the emplacement of the quartz monzonitic intrusions.

The U-Pb zircon data obtained from the quartz monzonite sample (HS-17) reveal concordant U-Pb ages that fall into two groups: the first one is based on the majority of zircon grains with a weighted mean $^{206}Pb/^{238}U$ age of 624.4 ± 4.5 Ma (MSWD = 0.17, 95% confidence interval). This age represents the magmatic age of the quartz monzonite intrusions in the study area (Fig. 5g). The second group displays a weighted mean $^{206}Pb/^{238}U$ age of 662.1 ± 6.9 Ma; MSWD = 0.24 (Fig. 5g) that is compatible with the age of the granitic rocks in the study area. We interpret this age as the emplacement age of the host granite.

In summary, the HSZ granitoid rocks define two age groups. The first group represents an older granitoid suite, which includes (in this study) granite and quartz syenite samples (HS-1 and HS-5), with weighted mean $^{206}Pb/^{238}U$ ages of 664.2 ± 3.8 Ma, and 662.1 ± 4.6 Ma, respectively. The average age for this older group is hence ~663 Ma (Fig. 5a, c). The second group, represented by the quartz monzonite samples (HS-15 and HS-17), displays weighted mean $^{206}Pb/^{238}U$ ages of 623.4 ± 3.6 Ma and 624.4 ± 4.5 Ma, respectively, with an average age of ~623.5 Ma (Fig. 5e, g). This Ediacaran age of quartz monzonite intrusions in the HSZ is consistent with the available ages from the post-collisional, Humr Akarim and Humrat Mukbid granitic plutons in the Eastern Desert of Eygpt (Ali et al., 2013).

Our geochronological data from the HSZ granitoid rocks are also significant to better constrain the timing of deformation in and across the Hamisana Shear Zone. Based on Rb-Sr and U-Pb zircon ages obtained from intrusive and gneissic rocks in the northern Hamisana Shear Zone, Stern et al. (1989) and Stern and Kröner (1993) suggested that this shear zone was actively deforming between 660 Ma and 550 Ma. However, our age data from undeformed quartz monzonite intrusions within the shear zone indicate that there was no active deformation in and across the Hamisana Shear Zone by 624 Ma.

9.2. Petrogenesis of HSZ granitoid magmas

The origin and melt evolution of magmas of the ANS granitoids are also poorly constrained (Ali et al., 2015). As different elements show different degrees of mobility during alteration and metamorphism, the original abundances of some elements in altered and deformed / metamorphosed magmatic rocks may have been moderately to significantly modified (Polat et al., 2003). Therefore, in order to discuss the origin of the magmas of the HSZ granitoids, it is imperative that we first evaluate the possible effects of secondary post-magmatic alteration, crustal contamination, and fractional crystallization on rock compositions.

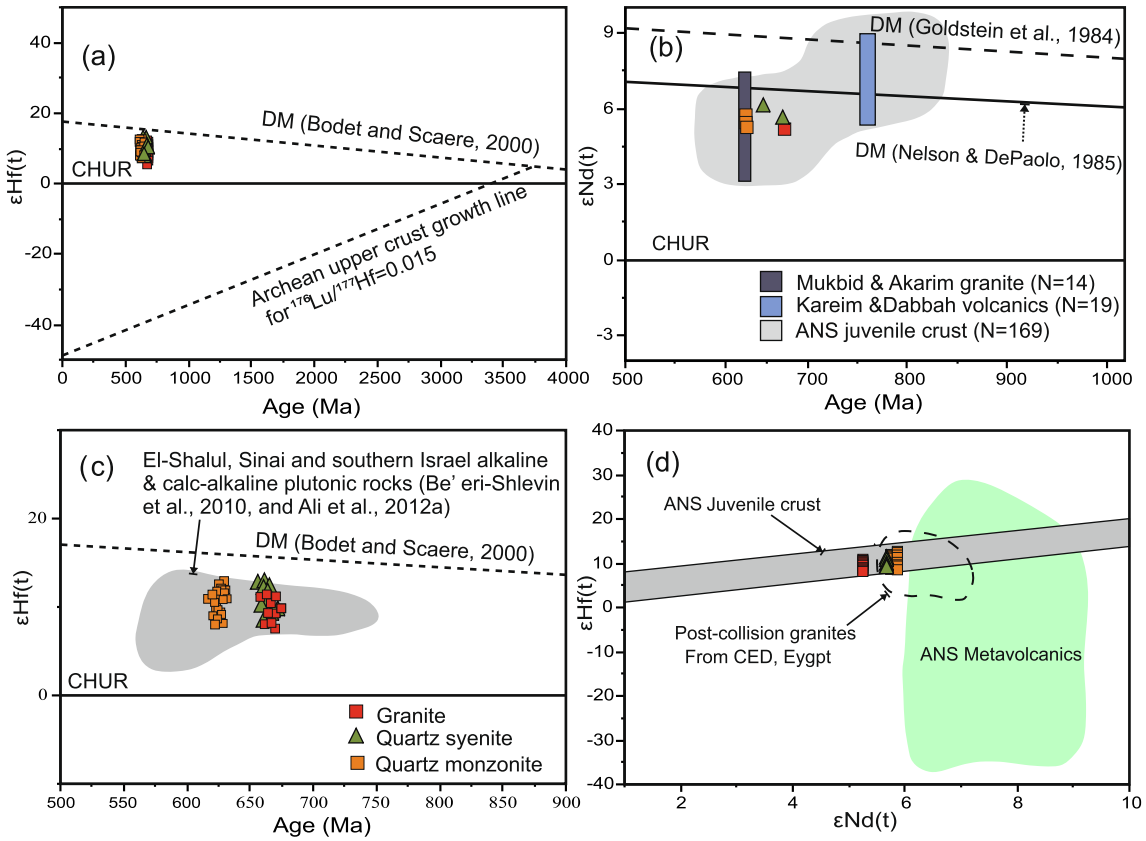

Fig. 12. (a and c) Epsilon Hf(t) versus zircon age diagrams showing zircon data for Neoproterozoic HSZ granitoids. Depleted mantle (DM) growth curve from Bodet and Scharer (2000). The field for El-Shalul (CED) granite, Sinai, Egypt, and southern Israel alkaline and calc-alkaline rocks is from Be'eri-Shlevin et al. (2010), and Ali et al. (2012a). CHUR = chondritic uniform reservoir. (b) Age vs. $\varepsilon_{Nd}(t)$ evolution diagram for Neoproterozoic HSZ granitoids. The reference line for the chondritic uniform reservoir (CHUR) and depleted mantle (DM) are from Goldstein et al. (1984), and Nelson and DePaolo (1985). Juvenile Neoproterozoic ANS field is from Hargrove et al. (2006b), Ali et al. (2009), Moussa et al. (2008), and Stoeser and Frost (2006); data for the Mukbid & Akarim granite and the Kareim & Dabbah volcanic suites are from Ali et al. (2012a and 2013) for comparison. (d) εNd(t) versus εHf(t) diagram. Juvenile crust field is from Ali et al. (2012a), Be'eri-Shlevin et al. (2010), Katz et al. (2004), and Vervoort and Blichert-Toft (1999). Fields for εNd(t)–εHf(t) in arc-metavolcanics and post-collisional granite from CED (Egypt) are from Ali et al. (2013).

The calc-alkaline HSZ granitoids display significant correlations of major elements with SiO_2 values on Harker diagrams (Fig. 8). This feature may argue against the role of magma mixing, as such correlations are considered a major cause of linear variation in Harker diagrams (cf. Wall et al. (1987), Chappell (1996)). Major oxides show different silica correlation trends (Fig. 8): MgO, CaO, TiO_2, Fe_2O_3t, Al_2O_3, and P_2O_5 display strong negative correlations, whereas Na_2O exhibit a slightly positive correlation. K_2O shows positive correlations with SiO_2. The observed negative correlations with SiO_2 may indicate that fractional crystallization might have affected the chemical compositions of the HSZ granitoid magmas slightly (e.g., Foley et al. (2002), Karsli et al. (2012)). The negative correlation between SiO_2 and TiO_2 or Fe_2O_3 may also indicate the separation of Fe-Ti oxides during crystallization (Karsli et al., 2012). The relatively consistent Eu values with Ba and Sr contents, negative Eu values with Y contents, and variable Ba and Rb values with Sr contents indicate that our quartz monzonite rock samples likely show attributes of K-feldspar and biotite crystallization. However, these features of the granite, granodiorite and quartz syenite samples may be attributed to residual plagioclase and amphibole rather than magmatic fractionation (Fig. 9). Nevertheless, these correlations strongly indicate that these element abundances reflect the original contents of the main mineral phases, and that post-magmatic alteration and metamorphism appear not to have changed the rock compositions significantly.

The HSZ granitoids display strong homogeneity in their geochemical (Table 1), and Hf, Sr-Nd isotopic features (Tables 3 and 4). The results of our Hf and Sr-Nd isotope analyses show no involvement of the pre-Neoproterozoic crust in the magmatic evolution of the HSZ granitoids. These findings are consistent with the previously published results of isotopic work (Nd–Sr–Pb) from the ANS (Stein and Goldstein, 1996; Stein, 2003; Be'eri-Shlevin et al., 2010). Thus, we can rule out any role of mixing and mingling processes in the evolution of the magmas of the HSZ granitoids.

High-degree fractional crystallization of mantle-derived mafic magmas may have potentially been involved in the formation of calc-alkaline granitoid rocks of the ANS. If this were the case, the ANS granitoid rocks should have contained mafic xenoliths (Weissman et al., 2013). However, large volumes of mafic magmas are typically required to produce even small amounts of silicic rocks through fractional crystallization (Medlin et al., 2015). Yet, the HSZ granitoids are the dominant plutonic rock types over a very limited mafic rock distribution in the study area (Fig. 1), and there are no mafic xenoliths found in the HSZ granitoids. These features argue strongly against fractional crystallization as the main petrogenetic process responsible for the formation of the HSZ granitoids. Furthermore, the La/Yb, La/Sm, and Th/Nb ratios are highly sensitive to magmatic processes and can thus be used to diagnose the partial melting versus fractional crystallization processes in melt evolution (Karsli et al., 2011; Yang et al., 2011). Although the analyzed granodiorite samples (undated) show no strong geochemical trends in support of partial melting or fractional crystallization, the granite, quartz syenite and quartz monzonite samples display a faint geochemical trend that appears compatible with partial melting (Fig. 10). Therefore, the observed geochemical trends of the HSZ granitoid samples are more consistent with partial melting than

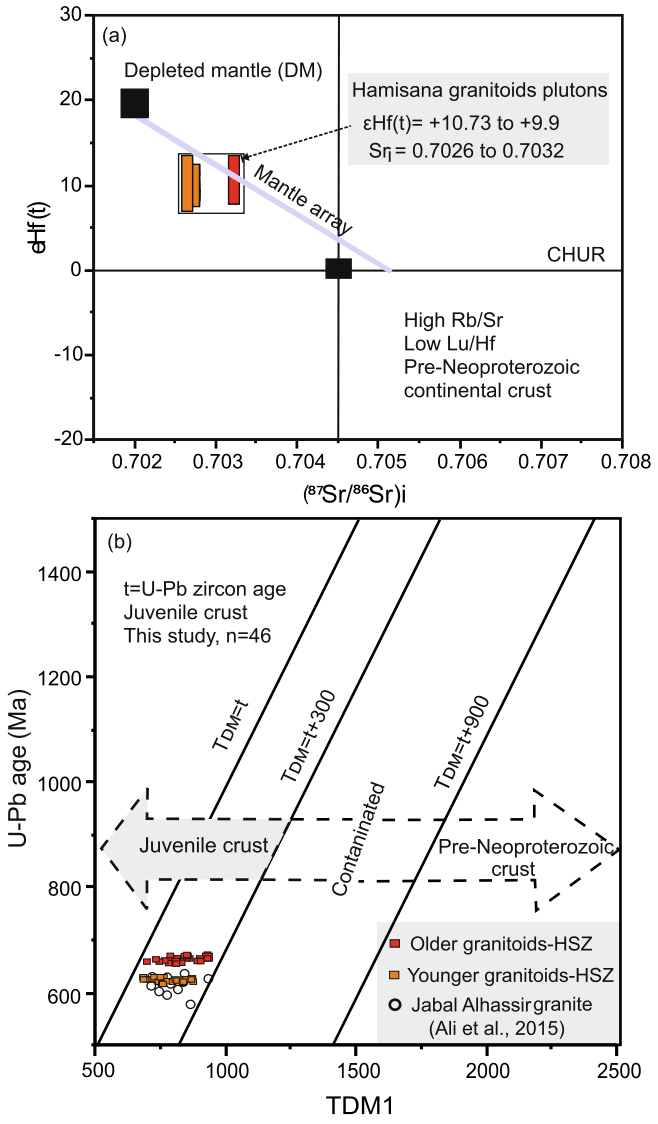

Fig. 13. (a) Plot of εHf(t) versus whole-rock initial $^{87}Sr/^{86}Sr$ (Sri) from the Neoproterozoic HSZ granitoid plutons which are similar to those of magmas derived from the Neoproterozoic depleted mantle. The mantle array (MORB) is defined by oceanic basalts and the bulk earth $^{87}Sr/^{86}Sr$ values after Patchett (1983). (b) Plot of U–Pb zircon ages versus TDM1. Data yielding Hf-TDM1 = t (U–Pb zircon age) or Hf-TDM1 < t are considered to be derived from a juvenile source, whereas those with t + 300 < Hf-TDM1 < t + 900 or with Hf-TDM1 > t + 900 are considered to represent juvenile crust contaminated by pre-Neoproterozoic crustal components. Data of Jabal Al-Hassir granitic rocks is from Ali et al. (2015) for comparison.

fractional crystallization process (Fig. 10a–c). A plot of Rb/Sr vs. Rb/Ba ratios also show patterns that are in support of the origin of the HSZ granitoid magmas from partial melting of a basaltic magma source (Fig. 10d). The heat required for partial melting may have been provided by mantle-derived, hot basaltic magmas near the base of the colder crust, resulting in crustal melting in the presence of heat and water (hydrous fluids). The source of water could be dehydration melting due to hydrous mineral breakdown. Variations in fH_2O could account for differences in the resultant magma compositions and the residual rock (Holloway and Burnham, 1972; Beard and Lofgren, 1989, 1991; Rushmer, 1991; Wolf and Wyllie, 1994). We infer, therefore, that the Neoproterozoic HSZ granitoids formed by partial melting of a depleted mantle mantle beneath the ANS.

9.3. Nature of the magma source of the HSZ granitoids

The HSZ granitoids exhibit strong enrichment in most incompatible elements, with discernable negative anomalies in Nb, La, P, and Ti and strong depletion in Ba, K, Pb and Sr in a primitive mantle normalized diagram (Fig. 7b) (e.g., Martin (1993)). These geochemical characteristics are typical of subduction-generated magmas. The quartz syenite samples show more depletion in Zr, Hf and more enrichment in Lu and Y, whereas the granodiorite samples exhibit more enrichment in all these elements compared with other granitoid samples. The chondrite normalized diagram displays no significant Eu anomaly (Fig. 7). All the analyzed HSZ granitoid samples plot in the field of *Volcanic Arc Granite* (VAG) in Rb vs. Y + Nb and Yb vs. Ta diagrams (Fig. 11a-b; Pearce and Peate, 1995), whereas the younger monzonitic rocks fall in the post-collision arc field (Fig. 11a, c, d).

Nd–Sr–O–Hf isotopic compositions are ideally the best tracers to evaluate the magma sources of the ANS granitoids (Patchett and Tatsumoto, 1981; Amelin et al., 1999; Vervoort and Blichert-Toft, 1999; Be'eri-Shlevin et al., 2010; Collins et al., 2011). Previously published data on Sm-Nd whole-rock isotopic values and initial $^{87}Sr/^{86}Sr$ ratios suggest that magmas that contributed to the continental crust of the ANS was derived from depleted mantle sources, with negligible input from older, pre-Neoproterozoic crust (Stern, 2002; Moussa et al., 2008; Be'eri-Shlevin et al., 2009a,b, 2010; Liégeois and Stern, 2010; Stern and Johnson, 2010; Morag et al., 2011, 2012; Ali et al., 2012b; Augland et al., 2012; Lundmark et al., 2012; Ali et al., 2014). However, pre-Neoproterozoic zircons are found abundantly in Cryogenian (~750 Ma) volcanic sequences (Ali et al., 2009; Stern and Johnson, 2010), indicating recycling of older crustal zircons into the mantle melt source of these extrusive rocks.

All samples from the HSZ granitoids show positive εNd values, ranging from +5.24 to +6.10, which plot in the same field of the ANS juvenile crust (Fig. 12). The melt source of the HSZ magmas was depleted in Nd relative to Sm, consistent with an interpretation that Nd evolved in a strongly depleted chemical reservoir, such as the upper mantle prior to the Neoproterozoic (Liégeois and Stern, 2010; Shang et al. 2010). The positive εNd values of all our granitoid samples argue against the involvement of a pre–Neoproterozoic continental crust in their magma genesis (Table 4). Consistently, the Nd model ages ranging from 794 Ma to 877 Ma, which are closely similar to or slightly older than the zircon ages we have obtained, indicate a juvenile nature. This observation suggests that juvenile material additions from the mantle dominated the petrogenetic evolution of the studied granitoids.

Behavior of the whole-rock Lu–Hf isotopic system in magmatic rocks closely parallels that of the whole-rock Sm–Nd system (Vervoort et al., 1996, Vervoort and Blichert-Toft, 1999) and of the whole-rock Rb–Sr system. However, Hf isotopes of zircon grains have advantages over the Sm-Nd whole-rock system as a tracer of magma source and petrogenetic processes (Patchett and Tatsumoto, 1981; Vervoort et al., 1996; Scherer et al., 2001; Belousova et al., 2006; Kinny and Maas, 2003; Dickin, 2005; Belousova et al., 2010; Ali et al., 2014, 2015). They also provide a valuable tool as reliable chronometers. The younger granitoid units in the HSZ display Hf single model TDM1 ages of 625–876 Ma (Table 3) and plot in the depleted mantle and juvenile crust fields (Fig. 12a, c), reminiscent of alkaline and calc-alkaline plutonic rocks in El-Shalul, Sinai and southern Israel (Be'eri-Shlevin et al., 2010) and the Humrat Mukbid and Humr Akarim granites in the central Eastern Desert of Egypt (Fig. 12b; Ali et al., 2012b). Our data show similar εNd(t) and εHf(t) values for the older and younger series of the HSZ granitoids, indicating a depleted-mantle source (juvenile crust) for their melt origin (Fig. 12d). The εNd(t) and single zircon εHf(t) values of the quartz syenite and the younger quartz monzonite samples plot consistently within the field of post-collisional granites in the Eastern Desert of Egypt (Be'eri-Shlevin et al., 2010; Ali et al., 2012a, 2013). Nevertheless, in the $(^{87}Sr/^{86}Sr)i$ vs. εHf(t) diagram (Fig. 13a), all HSZ granitoids fall in the depleted mantle array. When we plot the

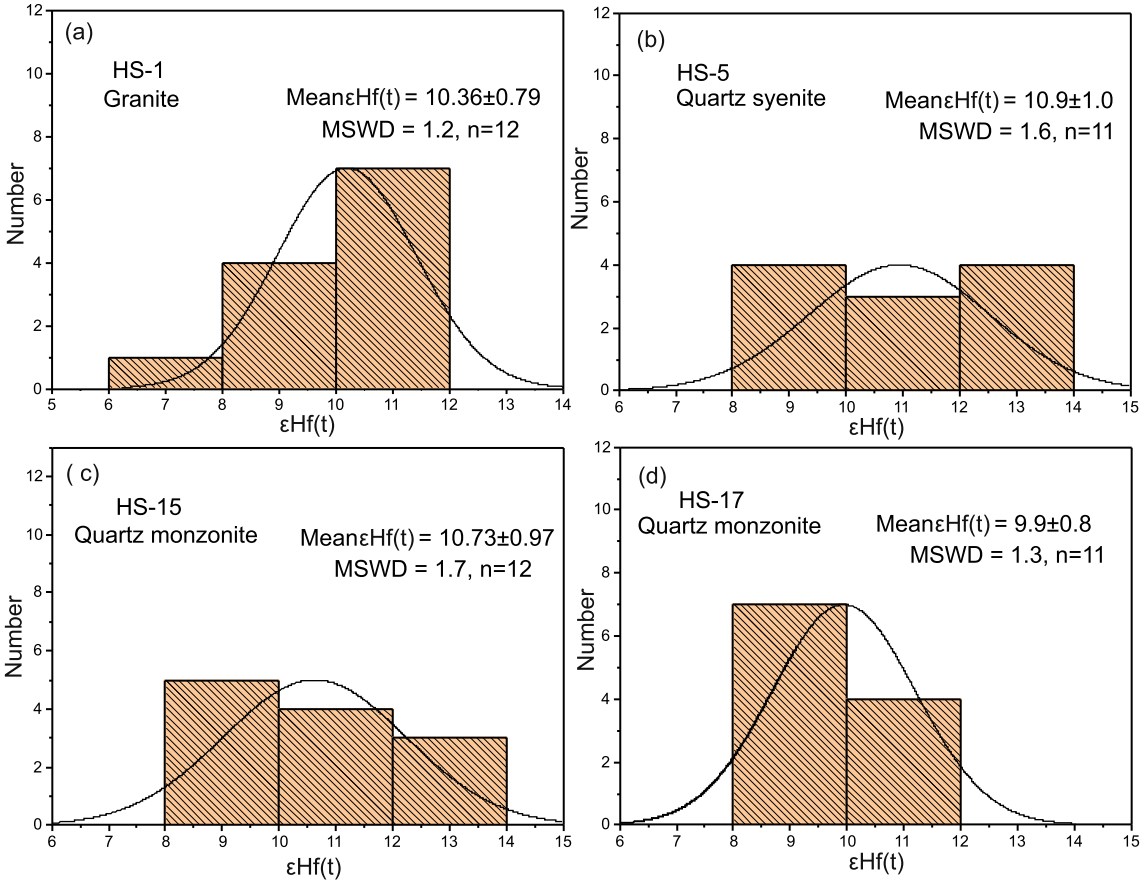

Fig. 14. Zircon $\varepsilon_{Hf}(t)$ values of granite (a), quartz syenite (b), and quartz monzonite (c, and d) for Neoproterozoic HSZ granitoids.

crystallization ages of the Neoproterozoic HSZ granitoids against the single model TDM1 ages, we also see that our samples fall into the juvenile crust field with no contamination effects of older material from the Pre–Neoproterozoic crust (Fig. 13b).

In-situ Hf isotopic results of the HSZ granitoid samples show positive εHf(t) values that are identical to a depleted-mantle source. The granite and quartz syenite samples have εHf(t) values ranging from 7.7 to 11.3 to 8.4–13.0, with average values of 10.36 and 10.9 (Fig. 14a, b), respectively. They show single model ages of 741–931 Ma and 735–895 Ma, respectively (Table 3). The quartz monzonite (younger granitoids) samples HS-15 and HS-17 have εHf(t) values of 8.1–13.0 and 8.3–11.95, with average values of 10.7 and 9.9 (Fig. 14c, d), respectively. The εHf(t) values of (+9.9) for the quartz monzonite is slightly less than those of the older granitoid suit, and this feature may indicate minor addition of melt from the underlying upper mantle. We posit that this event might have been caused by decompression melting of the upper mantle, following a lithospheric-scale delamination of the young and overthickened orogenic root after the continent–continent collision we have defined earlier (Eliwa et al., 2014).

10. Conclusions

The following conclusions can be drawn from this study, including the emplacement ages, the petrogenesis and melt sources, and the tectonic significance of the HSZ granitoids, which constitute a significance component of the ANS crust:

1. U–Pb zircon ages of the HSZ granitoids display two major groups: The older granitoids have weighted mean $^{206}Pb/^{238}U$ ages of 664.2 ± 3.8 Ma and 662.1 ± 4.6 Ma, with an average age of ~663 Ma. The younger granitoids, composed mainly of quartz monzonitic rocks, have emplacement ages of 623.4 ± 3.6 Ma and 624.4 ± 4.5 Ma, with an average age of ~623.5 Ma.
2. All HSZ granitoids show enrichment of LILEs and depletion of HFSEs, consistent with characteristic features of subduction-related magmas in a continental margin arc. The older granitic rocks represent pre-collisional volcanic arc products, whereas the younger quartz monzonitic rocks represent shoshonitic, post-collisional magmatic products.
3. Trace-element and REE ratios (La/Yb, La/Sm, Th/Nb, Rb/Sr, and Rb/Ba) of the HSZ granitoids indicate that their magmas formed from partial melting of a depleted mantle source beneath the ANS.
4. In-situ Hf isotope and Sr-Nd isotopic compositions of the HSZ granitoids have εHf(t) and εNd(t) values of + 10.36 to +10.9, and +5.24 to +6.1, respectively, which point to an identical depleted-mantle source and hence a juvenile-crust character with no involvement of pre-Neoproterozoic crust in their melt origin.
5. We infer that magmas of the HSZ granitoids were mainly derived from partial melting of a depleted mantle-derived juvenile mafic crust during the Neoproterozoic assembly of the Arabian-Nubian Shield.

Declaration of Competing Interest

The authors declare that they have no known competing financial interests or personal relationships that could have appeared to influence the work reported in this paper.

Acknowledgments

This study was supported by the National Natural Science Foundation of China under Grant No. 41230206. We are grateful to the

managers and the entire geological team of Pan Africa Maren Mining Co. Ltd., for providing us with logistical help and support during our fieldwork. We would like to express our appreciation for the support provided by the staff in the Department of Mineral Resources at Bahri University. We would like to thank Prof. Robert Stern (U.T. Dallas) for fruitful discussions on the geology of the ANS and for his valuable comments on our work in Sudan. We also thank Dr. Wan Le and Dr. Amjad Hussain for their assistance with isotopic analyses. We thank Editor Wilson Teixeira for his effective editorial handling of our manuscript, and the two anonymous reviewers for their insightful and constructive comments that helped us improve the paper.

Appendix A. Supplementary data

Supplementary data to this article can be found online at https://doi.org/10.1016/j.precamres.2020.105857.

References

Abdelsalam, M.G., Abdeen, M.M., Dowaidar, H.M., Stern, R.J., Abdelghaffar, A.A., 2003. Structural evolution of the Neoproterozoic western Allaqi-Heiani suture, southeastern Egypt. Precambr. Res. 124 (1), 87–104.

Abdelsalam, M.G., Stern, R.J., 1996. Structures and shear zones in the Arabian Shield. J. Afr. Earth Sci. 23, 289e310.

Adam, M.M.A., Lv, X., Abdel Rahman, A.A., and Stern, R.J., in press. In-situ sulfur isotope and trace element compositions of pyrite from the Haweit gold deposit, NE Sudan: Implications for the origin and source of the sulfur. Ore Geol. Rev..

Ali, K.A., Surour, A.A., Whitehouse, M.J., Andresen, A., 2015. Single zircon Hf–O isotope constraints on the origin of A-type granites from the Jabal Al-Hassir ring complex, Saudi Arabia. Precambr. Res. 256, 131–147.

Ali, K.A., Stern, R.J., Manton, W.I., Kimura, J.-I., Khamees, H.A., 2009. Geochemistry, Nd isotopes and U-Pb SHRIMP zircon dating of Neoproterozoic volcanic rocks from the Central Eastern Desert of Egypt: New insights into the ~750 Ma crust-forming event. Precambr. Res. 171 (1–4), 1–22.

Ali, K., Simon, W., Stern, R., Moghazi, A., Mahbubul Ameen, S. 2013. Hf isotopic composition of single zircons from Neoproterozoic post-collision granites, Eastern Desert of Egypt: implications for crustal growth and recycling in the Arabian-Nubian Shield. Precambr. Res. http://dx. doi. org/10.1016/j.precamres, 7.

Ali, K.A., Jeon, H., Andresen, A., Li, S.-Q., Harbi, H.M., Hegner, E., 2014. U-Pb zircon geochronology and Nd–Hf–O isotopic systematics of the Neoproterozoic Hadb adh Dayheen ring complex, Central Arabian Shield, Saudi Arabia. Lithos 206, 348–360.

Ali, K., Andresen, A., Manton, W.I., Stern, R.J., Omar, S.A., Maurice, A.E., 2012a. U-Pb zircon dating and Sr–Nd–Hf isotopic evidence to support a juvenile origin of the~ 634 Ma El Shalul granitic gneiss dome, Arabian-Nubian Shield. Geol. Mag. 149 (5), 783–797.

Ali, K.A., Moghazi, A.M., Maurice, A.E., Omar, S.A., Wang, Q., Wilde, S.A., Moussa, E.M., Manton, W.I., Stern, R.J., 2012b. Composition, age, and origin of the ~620 Ma Humr Akarim and Humrat Mukbid A-type granites: no evidence for pre-neoproterozoic basement in the Eastern Desert, Egypt. Int. J. Earth Sci. 101, 1705–1722.

Almond, D.C., Ahmed, F., 1987. Ductile shear zones in the northern Red Sea Hills, Sudan and their implication for crustal collision. Geol. J. 22 (S2), 175–184.

Altunkaynak, A., Sunal, G., Aldanmaz, E., Genc, C.S., Dilek, Y., Furnes, H., Foland, K.A., Yang, J.-S., Yildiz, M., 2012. Eocene granitic magmatism in NW Anatolia (Turkey) revisited: New implications from comparative zircon SHRIMPU-Pb and $^{40}Ar^{39}Ar$ geochronology and isotope geochemistry on magmagenesis and emplacement. Lithos 155, 289–309. https://doi.org/10.1016/j.lithos.2012.09.008.

Amelin, Y., Lee, D.C., Halliday, A.N., Pidgeon, R.T., 1999. Nature of the Earth's earliest crust from hafnium isotopes in single detrital zircons. Nature 399, 252–255.

Augland, L.E., Andresen, A., Boghdady, G.Y., 2012. U-Pb ID-TIMS dating of igneous and metaigneous rocks from the El-Sibai area: time constraints on the tectonic evolution of the Central Eastern Desert, Egypt. Int. J. Earth Sci. 101, 25–37.

Avigad, D., Gvirtzman, Z., 2009. Late Neoproterozoic rise and fall of the northern Arabian-Nubian Shield: the role of lithospheric mantle delamination and subsequent thermal subsidence. Tectonophysics 477, 217–228.

Beard, J.S., Lofgren, G.E., 1991. Dehydration melting and water-saturated melting of basaltic and andesitic greenstones and amphibolites at 1, 3, and 6. 9 kb. J. Petrol. 32(2), 365–401.

Beard, J.S., Lofgren, G.E., 1989. Effect of water on the composition of partial melts of greenstone and amphibolite. Science 244 (4901), 195–197.

Be'eri-Shlevin, Y., Katzir, Y., Valley, J.W., 2009a. Crustal evolution and recycling in a juvenile continent: oxygen isotope ratio of zircon in the northern Arabian Nubian Shield. Lithos 107, 169–184.

Be'eri-Shlevin, Y., Katzir, Y., Whitehouse, M.J., Kleinhanns, I.C., 2009b. Contribution of pre Pan-African crust to formation of the Arabian Nubian Shield: new secondary ionization mass spectrometry U-Pb and O studies of zircon. Geol. Soc. Am. 37, 899–902.

Be'eri-Shlevin, Y., Katzir, Y., Blichert-Toft, J., Kleinhanns, I.C. and Whitehouse, M.J., 2010. Nd–Sr–Hf–O isotope provinciality in the northernmost Arabian-Nubian Shield: implications for crustal evolution. Contrib. Mineral. Petro. 160(2), 181–201.

Be'eri-Shlevin, Y., Samuel, M.D., Azer, M.K., Ramo, O.T., Whitehouse, M.J., Moussa, H.E., 2011. The Ediacaran Ferani and Rutig volcano-sedimentary successions of the northernmost Arabian-Nubian Shield (ANS): new insights from zircon U-Pb geochronology, geochemistry and O-Nd isotope ratios. Precambr. Res. 188 (1–4), 21–44. https://doi.org/10.1016/j.precamres.2011.04.002.

Be'eri-Shlevin, Y., Eyal, M., Eyal, Y., Whitehouse, M.J., Litvinovsky, B., 2012. The Sa'al volcano-sedimentary complex (Sinai, Egypt): a latest Mesoproterozoic volcanic arc in the northern Arabian-Nubian shield. Geology 40, 403e406.

Belousova, E.A., Griffin, W.L., O'Reilly, S.Y., 2006. Zircon crystalmorphology, trace element signatures and Hf isotope composition as a tool for petrogeneticmodelling: examples from eastern Australian granitoids. J. Petrol. 47, 329–353.

Belousova, E., Kostitsyn, Y.A., Griffin, W.L., Begg, G.C., O'Reilly, S.Y., Pearson, N.J., 2010. The growth of the continental crust: constraints from zircon Hf-isotope data. Lithos 119, 457–466.

Bennett, J.D., Mosley, P.N., 1987. Current research in African earth sciences.

Blichert-Toft, J., Albaréde, F., 1997. The Lu–Hf geochemistry of chondrites and the evolution of the mantle–crust system. Earth Planet. Sci. Lett. 148, 243–258.

Bodet, F., Scharer, U., 2000. Evolution of the SE-Asian continent from U-Pb and Hfisotopes in single grains of zircon and baddeleyite from large River. Geochim. Cosmochim. Acta 64, 2067–2091.

Borg, L.E., Clynne, M.A., 1998. The petrogenesis of felsic calc alkaline magmas from southernmost Cascades, California: origin by partial melting of basaltic lower crust. J. Petrol. 39, 1197–1222.

Burke, K., Dewey, J., Kidd, W., 1977. World distribution of sutures—the sites of former oceans. Tectonophysics 40 (1–2), 69–99.

Chappell, B.W., 1996. Magma mixing and the production of compositional variation within granite suites: evidence from the granites of southeastern Australia. J. Petrol. 37 (3), 449–470.

Chappell, B.W., White, A.J.R., Wyborn, D., 1987. The importance of residual source material (restite) in granite petrogenesis. J. Petrol. 28, 1111–1138.

Chauvel, C., Levin, E., Carpentier, M., Arndt, N.T., Marini, J.-C., 2008. Role of recycledoceanic basalt and sediment in generating the Hf–Nd mantle array. Nat. Geosci. 1, 64–67.

Chu, N.C., Taylor, R.N., Chavagnac, V., Nesbitt, R.W., Boella, R.M., Milton, J.A., German, C.R., Bayon, G., Burton, K., 2002. Hf isotope ratio analysis using multi-collector inductively coupled plasma mass spectrometry: an evaluation of isobaric interference corrections. J. Anal. At. Spectrom. 17, 1567–1574.

Collins, A.S., Pisarevsky, S.A., 2005. Amalgamating eastern Gondwana: the evolutionof the Circum-Indian Orogens. Earth Sci. Rev. 71, 229–270.

Collins, W.J., Belousova, E.A., Kemp, A.I.S., Murphy, B.J., 2011. Two contrasting Phanerozoic orogenic systems revealed by hafnium isotope data. Nat. Geosci. 4, 333–337.

Davies, F.B., 1984. Strain analysis of wrench faults and collision tectonics of the Arabian-Nubian Shield. J. Geol. 92 (1), 37–53.

De La Roche, H., Leterrier, J., Grandclaude, P., Marchal, M., 1980. A classification of volcanic and plutonic rocks using R1R2-diagram and major-element analyses – its relationships with current nomenclature. Chem. Geol. 29, 183–210.

de Wall, H., Greiling, R.O., Sadek, M.F., 2001. Post-collisional shortening in the late Pan-African Hamisana high strain zone, SE Egypt: field and magnetic fabric evidence. Precambr. Res. 107 (3–4), 179–194.

Dhuime, B., Hawkesworth, C., Cawood, P., 2011. When continents formed. Science 331, 154155.

Dickin, A.P., 2005. Radiogenic Isotope Geology. Press Syndicate of the. University of Cambridge (492, pp.).

Dilek, Y., 2006. Collision tectonics of the Eastern Mediterranean region: Causes and consequences. In, Dilek, Y., Pavlides, Sp. (Eds.), Geological Society of America Special Paper 409, 1–13. doi:10.1130/2006.2409(1).

Dilek, Y., Thy, P., 1998. Structure, petrology, and seafloor spreading tectonics of the Kizildag ophiolite (Turkey). In: Mills, R., Harrison, K. (Eds.), Modern Ocean Floor Processes and the Geological Record, Geological Society of London Special Publication 148, 43–69.

Dilek, Y., Whitney, D.L., 2000. Cenozoic crustal evolution in central Anatolia: Extension, magmatism and landscape development. In: Proceedings of the Third International Conference on the Geology of the Eastern Mediterranean, Geological Survey Department, Nicosia–Cyprus, pp. 183–192.

Dilek, Y., Ahmed, Z., 2003. Proterozoic ophiolites of the Arabian Shield and their significance in Precambrian tectonics. In: Dilek, Y., Robinson, P.T. (Eds.), Ophiolite in Earth History. Geological Society, London, Special Publication, vol. 218, pp. 685–700.

Dilek, Y., Furnes, H., 2011. Ophiolite genesis and global tectonics: geochemical and tectonic fingerprinting of ancient oceanic lithosphere. Geol. Soc. Am. Bull. 123, 387–411. https://doi.org/10.1130/B30446.1.

Dilek, Y., Furnes, Y., 2014. Origins of ophiolites. Elements 10, 93–100. https://doi.org/10.2013/gselements.10.2.93.

Dilek, Y., Thy, P., Moores, E.M., Ramsden, T.W., 1990. Tectonic evolution of the Troodos ophiolite within the Tethyan framework. Tectonics 9 (4), 811–823.

El-Rahman, Y.A., Polat, A., Dilek, Y., Fryer, B.J., El-Sharkawy, M., Sakran, S., 2009a. Geochemistry and tectonic evolution of the Neoproterozoic incipient arc–forearc crust in the Fawakhir area, Central Eastern Desert of Egypt. Precambr. Res. 175 (1–4), 116–134.

El-Rahman, Y.A., Polat, A., Dilek, Y., Fryer, B., El-Sharkawy, M., Sakran, S., 2009b. Geochemical evolution of the Neoproterozoic Wadi Ghadir ophiolitic complex, Eastern Desert, Egypt. Lithos 113 (102), 158–178. https://doi.org/10.1016/j.lithos.2008.12.014.

Eliwa, H.A., El-Bialy, M.Z., Murata, M., 2014. Edicaran post-collisional volcanism in the Arabian-Nubian Shield: The high-K calc-alkaline Dokhan Volcanics of Gabal Samr El-Qaa (592 ± 5 Ma), North Eastern Desert, Egypt. Precambr. Res. 246, 180–207.

Farahat, E.S., Zaki, R., Hauzenberger, C., Sami, M., 2011. Neoproterozoic calc-alkaline peraluminous granitoids of the Deleihimmi pluton, Central Eastern Desert, Egypt: implications for transition from late-to post-collisional tectonomagmatic evolution in the northern Arabian-Nubian Shield. Geol. J. 46 (6), 544–560.
Farahat, E.S., Mohamed, H.A., Ahmed, A.F., El Mahallawi, M.M., 2007. Origin of I-and A-type granitoids from the Eastern Desert of Egypt: implications for crustal growth in the northern Arabian-Nubian Shield. J. Afr. Earth. Sci. 49 (1–2), 43–58.
Fritz, H., Abdelsalam, M., Ali, K.A., Bingen, B., Collins, A.S., Fowler, A.R., Ghebreb, W., Hauzenberger, C.A., Johnson, P.R., Kusky, T.M., Macey, P., Muhongon, S., Stern, R.J., Viola, G., 2013. Orogen styles in the East African Orogen: a review of the Neoproterozoic to Cambrian tectonic evolution. J. Afr. Earth Sci. 86, 65e106.
Foley, S., Tiepolo, M., Vannucci, R., 2002. Growth of early continental crust controlled by melting of amphibolite in subduction zones. Nature 417, 837–840.
Genna, A., Nehlig, P., Le Goff, E., Gguerrot, C., Shanti, M., 2002. Proterozoic tectonism of the Arabian Shield. Precambr. Res. 117, 21–40.
Goldstein, S.L., O'Nions, R.K., Hamilton, P.J., 1984. A Sm–Nd isotopic study of atmospheric dusts and particulates from major river systems. Earth Planet. Sci. Lett. 70, 221–236.
Griffin, W.L., Wang, X., Jackson, S.E., Pearson, N.J., O'Reilly, S.Y., Xu, X., Zhou, X., 2002. Zircons chemistry and magma genesis in SE China: in situ analysis of Hf isotopes, Pingtan and Tonglu igneous complexes. Lithos 61, 237–269.
Günther, D., Heinrich, A.C., 1999. Enhanced sensitivity in laser ablation-ICP mass spectrometry using helium-argon mixtures as aerosol carrier. J. Anal. Atomic Spectrom. 14(9), 1363–1368.
Hargrove, U.S., Stern, R.J., Griffin, W.R., Johnson, P.R., Abdelsalam, M.G., 2006a. FromIsland Arc to Craton: timescales of crustal formation along the neoprotero-zoic Bi'r Umq Suture zone, Kingdom of Saudi Arabia. Saudi Geol. Surv.Tech. Rep. SGS-TR-2006-6, 69.
Hargrove, U.S., Stern, R.J., Kimura, J.I., Manton, W.I., Johnson, P.R., 2006b. How juvenile is the Arabian-Nubian Shield? Evidence from Nd isotopes and pre-Neoproterozoic inherited zircon in the Bi'r Umq suture zone, Saudi Arabia. Earth Planet. Sci. Lett. 252, 308–326.
Holloway, J.R., Burnham, C.W., 1972. Melting relations of basalt with equilibrium water pressure less than total pressure. J. Petrol. 13 (1), 1–29.
Hu, Z., et al., 2014. "Wave" signal-smoothing and mercury-removing device for laser ablation quadrupole and multiple collector ICPMS analysis: application to lead isotope analysis. Anal. Chem. 87 (2), 1152–1157.
Huang, J., Zheng, Y.-F., Zhao, Z.-F., Wu, Y.-B., Zhou, J.-B., Liu, X., 2006. Melting of subducted continent: element and isotopic evidence for a genetic relationship between Neoproterozoic and Mesozoic granitoids in the Sulu orogen. Chem. Geol. 229, 227–256.
Jackson, S.E., Pearson, N.J., Griffin, W.L., Belousova, E.A., 2004. The application of laser ablation-inductively coupled plasma-mass spectrometry to in situ U-Pb zircon geochronology. Chem. Geol. 211 (1), 47–69.
Johnson, P.R., Andresen, A., Collins, A.S., Fowler, A.R., Fritz, H., Ghebreab, W., Kusky, T., Stern, R.J., 2011. Late Cryogenian-Ediacaran history of the Arabian-NubianShield: a review of depositional, plutonic, structural, and tectonic events in theclosing stages of the northern East African Orogen. J. Afr. Earth Sci. 61, 167–232.
Johnson, P.R., Abdelsalam, M.G., Stern, R.J., 2003. The Bi'r Umq-Nakasib suture zone in the Arabian-Nubian shield: a key to understanding crustal growth in the East African orogen. Gondwana Res. 6 (3), 523–530.
Johnson, P.R., 2014. An expanding Arabian-Nubian Shield geochronologic and isotopic dataset: defining limits and confirming the tectonic setting of a Neoproterozoic accretionary orogen. Open Geol. J. 8 (1).
Johnson, P.R., Woldehaimanot, B., 2003. Development of the Arabian-Nubian Shield: perspectives on accretion and deformation in the northern East African Orogenand assembly of Gondwana. In: Yoshida, M., Windley, B.F., Dasgupta, S. (Eds.), Proterozoic East Gondwana: Supercontinent Assembly and Breakup. J. Geol. Soc. Lond. Spec. Publ. 206, pp. 289–326.
Katz, O., Beyth, M., Miller, N., Stern, R.J., Avigad, D., Basu, A., Anbar, A., 2004. A lateNeoproterozoic (630 Ma) high-magnesium andesite suite from southern Israel:implication for the consolidation of Gondwanaland. Earth Planet. Sci. Lett. 218, 275–290.
Karsli, O., Uysal, I., Ketenci, M., Dokuz, A., Aydin, F., Kandemir, R., Wijbrans, J., 2011. Adakite-like granitoid porphyries in Eastern Pontides, NE Turkey: potential parental melts and geodynamic implications. Lithos 127, 354–372.
Karsli, O., Caran, S., Dokuz, A., Ban, H., Chen, B., Kandermir, R., 2012. A–ype granitoids from the Eastern Pontides, NE Turkey: records for generation of hybrid A-type rocks in a subduction-related environment. Tectonophysics 530–531, 208–224.
Kinny, P.D., Maas, R., 2003. Lu–Hf and Sm–Nd isotope systems in zircon. Rev. Mineral. Geochem. 53, 327–341. https://doi.org/10.2113/0530327.
Khalil, A.E.S., Obeid, M.A., Azer, M.K., 2015. Late Neoproterozoic post-collisional mafic magmatism in the Arabian-Nubian Shield: A case study from Wadi El-Mahash gabbroic intrusion in southeast Sinai, Egypt. J. Afr. Earth Sci. 105, 29–46. https://doi.org/10.1016/j.jafrearsci.2015.02.003.
Kröner, A., Grieling, R., Reischmann, T., Hussein, I., Stern, R., Dürr, S., Zimmer, M., 1987. Pan-African crustal evolution in the Nubian segment of northeast Africa. Proterozic Lithospheric Evol. 17, 235–257.
Kröner, A., 1985. Ophiolites and the evolution of tectonic boundaries in the late Proterozoic Arabian-Nubian Shield of northeastern Africa and Arabia. Precambr. Res. 27, 277–300.
Kröner, A., Linnebacher, P., Stern, R.J., Reischmann, T., Manton, W., Hussein, I.M., 1991. Evolution of Pan-African island arc assemblages in the southern Red Sea Hills, Sudan, and in southwestern Arabia as exemplified by geochemistry and geochronology. Precambr. Res. 53 (1–2), 99–118.
Lenting, C., Geisler, T., Gerdes, A., Koolman, E., Scherer, E., Zeh, A., 2010. The behav-ior of the Hf isotope system in radiation-damaged zircon during experimentalhydrothermal alteration. Am. Miner. 95, 1343–1348.
Liégeois, J.P., Stern, R.J., 2010. Sr–Nd isotopes and geochemistry of granite–gneiss complexes from the Meatiq and Hafafit domes, Eastern Desert, Egypt: No evidence for pre-Neoproterozoic crust. Int. J. Earth Sci. 57, 31–40.
Li, X.H., Li, Z.X., Li, W.X., Wang, X.C., Gao, Y.Y., 2013. Revisiting the "C-type adakites" of the Lower Yangtze River Belt, central eastern China: in-situ zircon Hf–O isotope and geochemical constraints. Chem. Geol. 345, 1–15.
Li, X.H., Long, W.G., Li, Q.L., Liu, Y., Zheng, Y.F., Yang, Y.H., Chamberlain, K.R., Wan, D.F., Guo, C.H., Wang, X.C., Tao, H., 2010. Penglai zircon megacrysts: a potential new working reference material for microbeam determination of Hf-O isotopes and U-Pb ages. Geostand. Geoanal. Res. 34, 117–134.
Lissan, N.H., Bakheit, A.K., 2010. The geology and geochemistry of metavolcanic rocks from Artoli Area, Berber Province, Northern Sudan: an implication for petrogenetic and tectonic setting. J. Am. Sci. 6 (8).
Liu, Y.S., Gao, S., Hu, Z.C., Gao, C.G., Zong, K.Q., Wang, D.B., 2010a. Continental and oceanic crust recycling-induced melt-peridotite interactions in the Trans-North China Orogen: U-Pb dating, Hf isotopes and trace elements in zircons of mantle xenoliths. J. Petrol. 51 (1&2), 537–571.
Liu, Y.S., Hu, Z.C., Zong, K.Q., Gao, C.G., Gao, S., Xu, J., Chen, H.H., 2010b. Reappraisement and refinement of zircon U-Pb isotope and trace element analyses by LA-ICP-MS. Chin. Sci. Bull. 55 (15), 1535–1546.
Liu, Y., Hu, Z., Gao, S., Guenther, D., Xu, J., Gao, C., Chen, H., 2008. In situ analysis of major and trace elements of anhydrous minerals by LA-ICP-MS without applying an internal standard. Chem. Geol. 257 (1–2), 34–43. https://doi.org/10.1016/j.chemgeo.2008.08.004.
Ludwig, K.R., 2003. ISOPLOT 3.00: A Geochronological Toolkit for Microsoft Excel. Berkeley Geochronology Center, California, Berkeley, p. 39.
Lundmark, A.M., Andresen, A., Hassan, M.A., Augland, L.E., Boghdady, G.Y., 2012. Repeated magmatic pulses in the East African Orogen in the Eastern Desert, Egypt: an old idea supported by new evidence. Gondwana Res. 22 (1), 227–237.
Luo, T., et al., 2018a. Reassessment of the influence of carrier gases He and Ar on signal intensities in 193nm excimer LA-ICP-MS analysis. J. Anal. At. Spectrom. 33 (10), 1655–1663.
Luo, T., et al., 2018b. Water vapor-assisted "universal" nonmatrix-matched analytical method for the in situ U-Pb dating of zircon, monazite, titanite, and xenotime by laser ablation-inductively coupled plasma mass spectrometry. Anal. Chem. 90 (15), 9016–9024.
Ma, Q., Zheng, J.P., Griffin, W.L., Zhang, M., Tang, H.Y., Su, Y.P., Ping, X.Q., 2012. Triassic "adakitic" rocks in an extensional setting (North China): melts from the cratonic lower crust. Lithos 149, 159–173.
Maniar, P.D., Piccoli, P.M., 1989. Tectonic discrimination of granitoids. Geol. Soc. Am. Bull. 101 (5), 635–643.
Martin, H., 1993. The mechanisms of petrogenesis of the Archaean continental crust—comparison with modern processes. Lithos 30 (3–4), 373–388.
McDonough, W.F., Sun, S.S., 1995. The composition of the Earth. Chem. Geol. 120 (3–4), 223–253.
Medlin, C.C., Jowitt, S.M., Cas, R.A.F., Smithies, H., Kirkland, C.L., Maas, R.A., Raveggi, M., Howard, H.M., Wingate, M.T.D., 2015. Petrogenesis of the A-type, mesoproterozoic intra-caldera rheomorphic kathleen ignimbrite and comagmatic rowland suite intrusions, West Musgrave Province, Central Australia: products of extreme fractional crystallization in a failed rift setting. J. Petrol. 56, 493–525.
Meert, J.G., 2003. A synopsis of events related to the assembly of eastern Gondwana. Tectonophysics 362 (1–4), 1–40. https://doi.org/10.1016/s0040-1951(02)00629-7.
Meyer, M., Klemd, R., Hegner, E., Konopelko, D., 2014. Subduction and exhumation mechanisms of ultra-high and high-pressure oceanic and continental crust at Makbal (Tianshan, Kazakhstan and Kyrgyzstan). J. Metamorph. Geol. 32 (8), 861–884.
Middlemost, E.A.K. 1985. Magmas and Magmatic Rocks, vol. 1. Longman, London, p. 266.
Middlemost, E.A., 1994. Naming materials in the magma/igneous rock system. Earth Sci. Rev. 37 (3–4), 215–224.
Miller, M.M., Dixon, T.H., 1992. Late Proterozoic evolution of the northern part of the Hamisana zone, northeast Sudan: constraints on Pan-African accretionary tectonics. J. Geol. Soc. 149 (5), 743–750.
Morag, N., Avigad, D., Gerdes, A., Belousova, E., Harlavan, Y., 2011. Crustal evolution and recycling in the northern Arabian-Nubian Shield: new perspectives from zircon Lu–Hf and U-Pb systematics. Precambr. Res. 186, 101–116.
Morag, N., Avigad, D., Gerdes, A., Harlavan, Y., 2012. 1000–580 crustal evolution in the northern Arabian-Shield revealed by U-Pb–Hf of detrital zircons from Late Neoproterozoic sediments. Precambr. Res. 208–211, 197–212.
Moussa, E.M.M., Stern, R.J., Manton, W.I., Ali, K.A., 2008. SHRIMP zircon datingand Sm/Nd isotopic investigations of Neoproterozoic granitoids, Eastern Desert, Egypt. Precambr. Res. 160, 341–356.
Nelson, B.K., DePaolo, D.J., 1985. Rapid production of continental crust 1.7 to 1.9 by ago: Nd isotopic evidence from the basement of the North American midcontinent. Geol. Soc. Am. Bull. 96, 746–754.
Pallister, J.S., Stacey, J.S., Fischer, L.B., Premo, W.R., 1988. Precambrian ophiolites of Arabia: Geologic settings, U- Pb geochronology, Pb-isotope characteristics, and implications for continental accretion. Precambr. Res. 38 (1), 1–54.
Patchett, P.J., Chase, C.G., 2002. Role of transform continental margins in major crustal growth episodes (vol 30, pg 39, 2002). Geology 30 (4), 384.
Patchett, P.J., 1983. Hafnium isotope results from mid-ocean ridges and Kerguelem. Lithos 16, 47–51.
Patchett, P.J., Tatsumoto, M., 1981. A routine high-precision method for Lu-Hf isotope geochemistry and chronology. Contrib. Miner. Petrol. 75 (3), 263–267.
Pearce, J.A., Harris, N.B., Tindle, A.G., 1984. Trace element discrimination diagrams for

the tectonic interpretation of granitic rocks. J. Petrol. 25 (4), 956–983.
Pearce, J.A., Peate, D.W., 1995. Tectonic implications of the composition of volcanic arc magmas. Annu. Rev. Earth Planet. Sci. 23 (1), 251–285.
Peccerillo, A., Taylor, S.R., 1976. Geochemistry of Eocene calc-alkaline volcanic rocks from the Kastamonu area, northern Turkey. Contrib. Miner. Petrol. 58 (1), 63–81.
Polat, A., Hofmann, A.W., Münker, C., Regelous, M., Appel, P.W., 2003. Contrasting geochemical patterns in the 3.7–3.8 Ga pillow basalt cores and rims, Isua greenstone belt, Southwest Greenland: implications for postmagmatic alteration processes. Geochim. Cosmochim. Acta 67 (3), 441–457.
Qi, L., Hu, J., Gregoire, D.C., 2000. Determination of trace elements in granites by inductively coupled plasma mass spectrometry. Talanta 51, 507–513.
Rushmer, T., 1991. Partial melting of two amphibolites: contrasting experimental results under fluid-absent conditions. Contrib. Miner. Petrol. 107 (1), 41–59.
Sláma, J., Košler, J., Condon, D.J., Crowley, J.L., Gerdes, A., Hanchar, J.M., Horstwood, M.S.A., Morris, G.A., Nasdala, L., Norberg, N., Schaltegger, U., Schoene, B., Tubrett, M.N., Whitehouse, M.J., 2008. Plešovice zircon-a new natural reference material for U-Pb and Hf isotopic microanalysis. Chem. Geol. 249, 1–35.
Scherer, E.E., Münker, C., Mezger, K., 2001. Calibration of the lutetium–hafniumclock. Science 293, 683–687.
Scherer, E.E., Whitwhouse, M.J., Münker, C., 2007. Zircons as a monitor of crustalgrowth. Elements 3, 19–24.
Shackleton, R.M., 1986. Precambrian collision tectonics in Africa. Geol. Soc. Lond. Spec. Publ. 19 (1), 329–349.
Shang, C.K., Morteani, G., Satir, M., Taubald, H., 2010. Neoproterozoic continental growth prior to Gondwana assembly: constraints from zircon–titanite geochronology, geochemistry and petrography of ring complex granitoids, Sudan. Lithos 118, 61–81.
Stacey, J., Agar, R.A., 1985. U-Pb isotopic evidence for the accretion of a continental microplate in the Zalm region of the Saudi Arabian Shield. J. Geol. Soc. 142 (6), 1189–1203.
Stein, M., Goldstein, S.L., 1996. From plume head to continental lithosphere in the Arabian-Nubian shield. Nature 382 (6594), 773–778. https://doi.org/10.1038/382773a0.
Stein, M., 2003. Tracing the plume material in the Arabian-Nubian Shield. Precambr. Res. 123 (2–4), 223–234.
Stern, R.J., Johnson, P.R., Kröner, A., Yibas, B., 2004. Neoproterozoic ophiolites ofthe Arabian-Nubian Shield. In: Kusky, T.M. (Ed.), Precambrian Ophiolites and Related Rocks. Developments in Precambrian Geology, vol. 13. Elsevier, Amsterdam, pp. 95–128.
Stern, R.J., Kröner, A., 1993. Geochronologic and isotopic constraints on Late Precambrian crustal evolution in NE Sudan. J. Geol. 101 (555–574), 1993.
Stern, R.J., Johnson, P.R., 2010. Continental lithosphere of the Arabian Plate: a geologic, petrologic, and geophysical synthesis. Earth Sci. Rev. 101, 29–67.
Stern, R.J., 2002. Crustal evolution in the East African Orogen: a Neodymium isotopic perspective. J. Afr. Earth Sci. 34, 109–117.
Stern, R.J., Nielsen, K.C., Best, E., Sultan, M., Arvidson, R.E., Kröner, A., 1990. Orientation of late Precambrian sutures in the Arabian-Nubian shield. Geology 18 (11), 1103–1106.
Stern, R., Kröner, A., Manton, W., Reischmann, T., Mansour, M., Hussein, I., 1989. Geochronology of the late Precambrian Hamisana shear zone, Red Sea Hills, Sudan and Egypt. J. Geol. Soc. 146 (6), 1017–1029.
Stern, R.J., 1994. Arc assembly and continental collision in the Neoproterozoic East African Orogen: implications for the consolidation of Gondwanaland. Annu. Rev. Earth Planet. Sci. 22 (1), 319–351.
Stern, R.J., Dawoud, A.S., 1991. Late Precambrian (740 Ma) charnockite, enderbite, and granite from Jebel Moya, Sudan: a link between the Mozambique Belt and the Arabian-Nubian Shield? J. Geol. 99 (5), 649–659.
Stoeser, D.B., Camp, V.E., 1985. Pan-African microplate accretion of the Arabian Shield. Geol. Soc. Am. Bull. 96 (7), 817–826.
Stoeser, D.B., Frost, C.D., 2006. Nd, Pb, Sr, and O isotopic characterization of Saudi Arabian shield terranes. Chem. Geol. 226 (3–4), 163–188. https://doi.org/10.1016/j.chemgeo.2005.09.019.
Sun, S.-S., McDonough, W.-S., 1989. Chemical and isotopic systematics of oceanic basalts: implications for mantle composition and processes. Geol. Soc. Lond., Spec. Publ. 42 (1), 313–345.
Taylor, S.R., McLennan, S.M., 1991. The Continental Crust: Its Composition and Evolution. Blackwell Scientific Publications, Oxford, p. 312.
Vail, J.R., 1985. Alkaline ring complexes in Sudan. J. Afr. Earth. Sci. 3 (1–2), 51–59. https://doi.org/10.1016/0899-5362(85)90022-3.
Vervoort, J.D., Patchett, P.J., Gehrels, G.E., Nutman, A.P., 1996. Constraints on early Earth differentiation from hafnium and neodymium isotopes. Nature 379, 624–627.
Vervoort, J.D., Blichert-Toft, J., 1999. Evolution of the depleted mantle: Hf isotope evidence from juvenile rocks through time. Geochim. Cosmochim. Acta 63, 533–556.
Wall, V.J., Clemens, J.D., Clarke, D.B., 1987. Models for granitoid evolution and source compositions. J. Geol. 95 (6), 731–749.
Wang, H., Wu, Y.B., Qin, Z.W., Zhu, L.Q., Liu, Q., Liu, X.C., Gao, S., Wijbrans, J.R., Zhou, L., Gong, H.J., Yuan, H.L., 2013. Age and geochemistry of Silurian gabbroic rocks in the Tongbai orogen, Central China: implications for the geodynamic evolution of the North Qinling arc-back-arc system. Lithos 179, 1–15.
Watson, E.B., 1996. Surface enrichment and trace-element uptake during crystal growth. Geochim. Cosmochim. Acta 60 (24), 5013–5020.
Watson, E.B., Cherniak, D.J., 1997. Oxygen diffusion in zircon. Earth Planet. Sci. Lett. 148 (3–4), 527–544.
Weissman, A., Kessel, R., Navon, O., Stein, M., 2013. The petrogenesis of calc-alkaline granites from the Elat massif, Northern Arabian-Nubian shield. Precambr. Res. 236, 252–264.
Wiedenbeck, M., et al., 1995. Three natural zircon standards for U-Th-Pb, Lu-Hf, trace element and REE analysis. Geostandards Newsletter 19 (1), 1–23.
Wolf, M.B., Wyllie, P.J., 1994. Dehydration-melting of amphibolite at 10 kbar: the effects of temperature and time. Contrib. Miner. Petrol. 115 (4), 369–383.
Wu, F.Y., Yang, Y.H., Xie, L.W., Yang, J.H., Xu, P., 2006. Hf isotopic compositions of the standard zircons and baddeleyites used in U-Pb geochronology. Chem. Geol. 234, 105–126.
Wu, Y., Zheng, Y., 2004. Genesis of zircon and its constraints on interpretation of U-Pb age. Chin. Sci. Bull. 49 (15), 1554–1569.
Wu, Y.B., Gao, S., Zhang, H.F., Yang, S.H., Jiao, W.F., Liu, Y.S., Yuan, H.L., 2008. Timing of UHP metamorphismin the Hong' an area, western DabieMountains, China: evidence from zircon U-Pb age, trace element and Hf isotope composition. Contrib. Mineral. Petrol. 155, 123–133.
Wyllie, P.J., Huang, W., Stern, C.R., Maaloe, S., 1976. Granitic magmas: possible and impossible sources, water contents, and crystallization sequences. Can. J. Earth Sci. 13, 1007–1019.
Wyllie, P.J., 1984. Sources of granitoid magmas at convergent plate boundaries. Phys. Earth Planet. Inter. 35, 12–18.
Xu, P., Wu, F.Y., Xie, L.W., Yang, Y.H., 2004. Hf isotopic compositions of the standard zircons for U-Pb dating. Chin. Sci. Bull. 49, 1642–1648.
Yang, B.H., Zhang, C.L., Li, L., 2011. Sr–Nd–Pb isotopic characteristics of the granitoids in the Douling complexes, eastern Qinling, China and its geological significance. Geol. Bull. China 30, 439–447.
Yuan, H.L., Gao, S., Dai, M.N., Zong, C.L., Gunther, D., Fontaine, G.H., Liu, X.M., Diwu, C., 2008. Simultaneous determinations of U-Pb age, Hf isotopes and trace element compositions of zircon by excimer laser-ablation quadrupole and multiple-collector ICPMS. Chem. Geol. 247, 100–118.
Zoheir, B.A., Johnson, P.R., Goldfarb, R.J., Klemm, D.D., 2019. Orogenic gold in the Egyptian Eastern Desert: widespread gold mineralization in the late stages of Neoproterozoic orogeny. Gondwana Res.